

Scalable multi-qubit intrinsic gates in quantum dot arrays

Jiaan Qi^{1,*}, Zhi-Hai Liu^{1,†} and Honqi Xu^{1,2,‡}

¹*Beijing Academy of Quantum Information Sciences, Beijing 100193, China*

²*Beijing Key Laboratory of Quantum Devices, Key Laboratory for the Physics and Chemistry of Nanodevices, and School of Electronics, Peking University, Beijing 100871, China*

(Dated: March 12, 2024)

We study the multi-qubit quantum gates intrinsic to a general array of semiconductor quantum dots and investigate how they can be implemented in a scalable way. The intrinsic quantum gates refer to the class of natural-forming transformations in the qubit rotating-frame under direct exchange coupling, and can be recognized as the instruction set of a spin-qubit chip. Adopting an perturbative treatment, we can model intrinsic gates by first-order dynamics in the coupling strength. A general formalism is developed for identifying the multi-qubit intrinsic gates under arbitrary array connectivity. Factors influencing the fidelities of the multi-qubit intrinsic gates are discussed. The advantageous applications of intrinsic gates in quantum computing and quantum error correction are explored. We also propose a theoretical scheme to overcome the problem of inhomogeneous coupling using dynamical calibration of the connecting bonds. This scheme can be further combined with periodic dynamical decoupling for robust implementations of multi-qubit gates in large-scale quantum computers.

I. INTRODUCTION

Semiconductor quantum dots are promising physical platforms for universal quantum computing [1–4]. The spins of electrons (or holes) are natural two-level systems that can be selectively manipulated and brought into interactions by confining them with artificial structures. Spin qubits defined in quantum dots enjoy several unique advantages, including their small physical size and compatibility with modern semiconductor fabrication techniques, that make them suitable for creating large-scale quantum chips [5, 6]. Under intensive research efforts from the global community, the technologies and theories behind spin qubits have seen significant advancements over recent years. Continuous developments in key performance metrics such as the coherence times, operation frequencies and gate fidelities have been made [7]. Spin qubits in the state-of-the-art can be prepared and measured with fidelity exceeding 99% [8], manipulated at frequency over 540 MHz [9] and work in temperature above 4K [10]. The fidelity figures for single-qubit and two-qubit gates have been pushed beyond the fault-tolerance threshold value [11, 12]. Industrial manufacturing have also been demonstrated for quantum dot arrays [13, 14].

The natural roadmap of any quantum computing scheme is to incorporate gradually increasing quantities of qubits for realizing useful quantum algorithms. However, accurate control of multiple qubits can be a highly nontrivial task that implies much more than just putting the qubits together. For selective control of the interqubit coupling, one must be able to eliminate the crosstalk effects of the control signals in an efficient manner. In addition, there must be a robust method to overcome

the inhomogeneous coupling across the qubits. The key challenge is that the relevant control resources must scale well with the number of qubits, for potential application to large-scale chips with millions of qubits. For spin qubits, a viable way to scale up the qubit count is to employ an increasing two-dimensional array of quantum dots, as recently demonstrated for crossbar arrays of hole qubits [15–18]. This configuration is also compatible with the surface code, a topological error correction code commonly conceived as the framework for large-scale fault-tolerant quantum computers [19–21]. The ability to control and optimize such a multi-qubit array necessarily marks the next milestone in spin qubits.

Analogous to how the basic instruction sets for different classical CPU architectures are different, quantum computers also have platform-dependent instruction sets. The general quantum computing theory favors controlled-not (CNOT) as the universal two-qubit gate [22]. Any algorithm may nevertheless be carried out with a different set of universal gates. For the best performance, a quantum algorithm should be compiled with the most natural gates for the physical platform it is applied upon. For spin qubits in particular, we consider a quantum gate as intrinsic if it can be attained with a single-step evolution under exchange interaction only. The controlled-phase (CPhase) or in particular controlled-Z (CZ) gate is an intrinsic two-qubit gate as it can be performed by simply turning on the exchange coupling [23–25]. In comparison, the CNOT gate for spin qubits is not intrinsic by our definition as it relies on external microwave drive to resonantly select the transition states [26]. In general, the “DC control” for CZ gate is less susceptible to noise compared with the “AC control” for CNOT [27–29], and is arguably easier to control and calibrate. Moreover, intrinsic gates need not be limited to two qubits. Most quantum algorithms require imposing joint transformations on multiple qubits. In these scenarios, intrinsic multi-qubit gates can often be used in place

* qija@baqis.ac.cn

† liuzh@baqis.ac.cn

‡ hqxu@pku.edu.cn

of equivalent clusters of single-qubit and two-qubit gates. Such replacements can boost efficiency, reducing control expenditures, while also less prone to errors [30]. Giving these obvious benefits, an abundance of recent studies have been devoted to multi-qubit gates in various systems such as Rydberg atoms [31–34], superconducting qubits [30, 35–37] and trapped ions [38, 39]. For spin qubits, three-qubit Toffoli gate have been proposed and implemented using resonant microwave pulse [40, 41]. Notably, studies on linear quantum dot chains have revealed coherent “superexchange” oscillations of the boundary states [42, 43], and exhibit long-range coupling [44, 45]. These studies clearly demonstrate the possibility of multi-qubit gates with DC control and hint a larger class of intrinsic multi-qubit gates.

Spin arrays coupled by exchange interaction have long fascinated theoretical investigations [46–50]. However, to-date it is still unclear what and how multi-qubit gates can be achieved in general. In this paper, we fill this important gap in current research with a comprehensive study on the qubit dynamics of quantum dot arrays. Extending the theoretical formalisms developed in an earlier paper [51], we greatly generalize the CZ/CPhase gate to a large class of multi-qubit gates intrinsically accessible to spin qubits. Furthermore, we also show these multi-qubit gates are scalable by proposing an efficient theoretical scheme to dynamically calibrate and control the inter-qubit couplings. While minimizing the crosstalk problem for selective controls, our scheme can also simultaneously protect the qubits from environmental couplings. Hopefully, our findings can pave the way for future large-scale quantum computing using spin qubits.

This paper is organized as follows. Section II goes through the theoretical prerequisites for the study of intrinsic gates. These include the entangled-state representation of the effective Hamiltonian, followed by introduction of the qubit frame, where quantum gates are formally derived and extended with additional free phase gates. In section III, we look into the class of all possible multi-qubit intrinsic gates defined on a quantum dot array with any geometry. It turns out that there is a surprisingly easy way of decomposing them. We estimate the coherent fidelity of these multi-qubit gates and discuss their potential applications in quantum computation and quantum error correction. In section IV, we examine the unavoidable problem of inhomogeneous coupling brought by scaling up the system. We propose a theoretical scheme to dynamically calibrate the bonds by applying single-qubit pulses. These scheme can be further combined with various dynamical decoupling protocols [52–54] in a suitable way that protect the spin qubits from environmental noise. Finally, we discuss a technical prospect implied by our theory where the interdot coupling can be efficiently controlled by tuning the local spin-orbital coupling strength. We summarize and conclude in section V.

II. DYNAMICS OF THE DOT ARRAY

Let us consider a spin-qubit chip defined in a semiconductor nanostructure using an array of quantum dots. An example set up is illustrated in Fig. 1(a) for a two-dimensional grid of quantum dots. The dots can also form a one-dimensional chain or even a three-dimensional lattice. Here we will use the general expression of “array” irrespective of the dimensionality. The dot array has suitable confining and chemical potentials that capture free charge carriers (electrons or holes) in the half-filling regime, i.e., only a single charge carrier occupies the lowest-energy orbit of each dot. A static magnetic field is applied to the system, lifting the two-fold spin degeneracy of the ground-level orbits and allowing localized spin qubits to be associated with the dots.

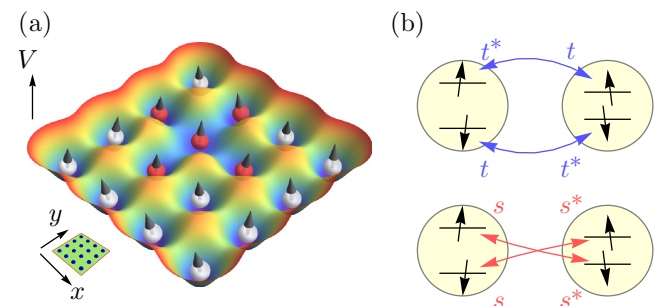


FIG. 1. (a) The potential profile of a two-dimensional array of quantum dots serving as a prototypical spin qubit quantum chip (left-bottom inset). Localized charge carriers with spins are represented as small balls with arrows. The red balls are in an active region where multiple spins are simultaneously coupled together for a multi-qubit gate. (b) Schematic plot of the spin qubits and the interdot coupling through virtual tunneling. Each qubit is defined by the lowest-energy spin-split states localized to a dot. The coefficients representing 8 possible tunneling process can be reduced to only two complex numbers due to symmetry—the spin conserved tunnelling t and spin-flipped tunnelling s .

The semiconducting device is assumed to have considerable spin-orbital interaction (SOI) to enable fast manipulation of single spin states with electric signals [55]. The SOI can be either intrinsic to the nanostructure [56] or artificially introduced by slanting magnetic field [57]. In general, the dots can have different Landé g -factors with different principal axes, hence the spatial spin directions and Zeeman energy splittings for the $|\uparrow\rangle$ and $|\downarrow\rangle$ states can differ across the dots. Electronic tunneling is allowed among neighboring sites. But the immediate state after tunneling involves two spins occupying the same dot and is not energetically favored due to a large Coulomb repulsion energy. The theory of quantum mechanics, however, allows brief transition to such high energy states in a process known as virtual tunneling. This is assumed to be the main mechanism for the exchange interaction between spin qubits.

A. Entangled state representation of the effective Hamiltonian

The Fermi-Hubbard model is a good starting point describing such quantum dot array [58, 59]. The low-energy states localized to all the dots can be normalized to form a basis $\{|\phi_{j,\sigma}\rangle\}$, where j represents the dot location and $\sigma \in \{\uparrow, \downarrow\}$ is the spin index. Using the annihilation $a_{j\sigma}$ and creation $a_{j\sigma}^\dagger$ operators for the basis states, one can write down a second-quantized Hamiltonian for the dot array. We split this Hamiltonian into a dot part and a tunnel-coupling part $H = H_{\text{dot}} + H_{\text{ex}}$. The dot part describes the energy costs for filling 0 to 2 spins into the ground-level orbit to each dot,

$$H_{\text{dot}} = \sum_{j\sigma} \left[(\mu_j + \text{sig}(\sigma_j) \frac{1}{2} \varepsilon_{Z,j}) n_{j\sigma} + \frac{1}{2} U n_{j\sigma} n_{j\bar{\sigma}} \right], \quad (1)$$

where $n_{j\sigma} = a_{j\sigma}^\dagger a_{j\sigma}$ is the number operator, μ_j and $\varepsilon_{Z,j}$ are the local chemical potential and the electron Zeeman energy at site j , the spin sign is defined by $\text{sig}(\uparrow\downarrow) = \pm 1$ and U is the energy cost for filling two antiparallel spins into the same orbit. The tunneling part is given by,

$$H_{\text{ex}} = \sum_{\langle j,k \rangle} \sum_{\sigma} \left(t_{\sigma\sigma}^{jk} a_{j\sigma}^\dagger a_{k\sigma} + s_{\sigma\bar{\sigma}}^{jk} a_{j\sigma}^\dagger a_{k\bar{\sigma}} \right), \quad (2)$$

where $t_{\sigma\sigma}^{jk}$ and $s_{\sigma\bar{\sigma}}^{jk}$ represent the spin dependent tunneling coefficients between adjacent dots j, k . We note that SOI mixes the orbit and the spin wave functions, while also opening a spin-flipping channel when tunneling among the dots [60].

Examining the spin-dependent tunneling process, for example, among dot j and k . There are four spin conserved coefficients in addition to four spin flipped terms due to SOI and differences in spin axes. A key assumption for our theory is that the time reversal symmetry is approximately preserved for our system. This requires the Zeeman splitting energy to be much smaller than the characteristic barrier height between the dots. Hermicity of the Hamiltonian and well as time reversal symmetry implies that only two independent coefficients exists: the spin-conserved tunneling coefficient and spin-flipped tunneling coefficient,

$$\begin{aligned} t_{j\downarrow, k\downarrow} &= t_{k\uparrow, j\uparrow} = (t_{j\uparrow, k\uparrow})^* = (t_{k\downarrow, j\downarrow})^* \propto t_{\langle jk \rangle}, \\ s_{j\downarrow, k\uparrow} &= s_{j\uparrow, k\downarrow} = (s_{j\downarrow, k\uparrow})^* = (s_{k\uparrow, j\downarrow})^* \propto s_{\langle jk \rangle}, \end{aligned} \quad (3)$$

where we have introduced dimensionless coefficients for spin-conserved (t) and spin-flipped (s) tunneling. They satisfy the normalization condition $|t|^2 + |s|^2 = 1$. In particular, in systems where direct-exchange dominates and g factors are scalar, we can have the explicit parametrization $t = \cos(\gamma_{\text{SO}}) - i \sin(\gamma_{\text{SO}}) \cos(\vartheta_B)$ and $s = -i \sin(\gamma_{\text{SO}}) \sin(\vartheta_B)$ [51], where γ_{SO} and ϑ_B characterize the SOI strength and the effective magnetic field angle. These relations make it possible to experimentally control the values of t and s by varying the SOI strength.

The normalized tunneling coefficients uniquely determines an entangled state $|\xi_w\rangle_{\langle j,k \rangle}$ that lives on the four-dimensional Hilbert space defined by the half-filling states of the connecting vertices,

$$|\xi_w\rangle = \frac{1}{\sqrt{2}} \left(s_w^* |\uparrow\uparrow\rangle_w + t_w^* |\uparrow\downarrow\rangle_w - t_w |\downarrow\uparrow\rangle_w + s_w |\downarrow\downarrow\rangle_w \right). \quad (4)$$

With this entangled state defined, the rule to write down the computational Hamiltonian is handy,

$$H = H_{\text{dot}} + H_{\text{ex}} = \sum_j \frac{1}{2} \varepsilon_j^Z \sigma_j^Z - \sum_w J_w |\xi_w\rangle \langle \xi_w|, \quad (5)$$

where H_{dot} is the Hamiltonian of the quantum dots, which is the summation of the effective Zeeman splitting energies ε_j^Z along the Pauli operator $\sigma_j^Z = |\uparrow\rangle\langle\uparrow|_j - |\downarrow\rangle\langle\downarrow|_j$ of all individual dots. The exchange term H_{ex} describes the coupling among connecting dots (edges). The coupling strength is specified by its exchange energy,

$$J_{\langle j,k \rangle} = \frac{T_{jk}}{2} \left(\frac{1}{U - \mu_j + \mu_k} + \frac{1}{U - \mu_k + \mu_j} \right), \quad (6)$$

which is a function of the tunneling amplitude, dot charging energy and the chemical potentials of the connecting dots. Equation (5) represents the effect of direct exchange in terms the entangled-state representation. We explicitly derive it in the Supplementary Material. Besides mathematically compact, the entangled-state representation of has many nice properties that we will take advantage of in the development of multi-qubit gates.

B. Time evolution in the qubit frame

In general, the Hamiltonian governing dynamics of qubits can be split as $H = H_0 + H_1$, where H_0 is the intrinsic Hamiltonian, or self-energy, required for the proper definition of qubits, and H_1 includes all other interactions and control signals. The intrinsic Hamiltonian is persistent and applies the unitary rotation $U_0(\tau) = e^{-iH_0\tau}$ to the lab-frame quantum states. This unitary rotation defines the qubit frame, in which qubit states are stationary in absence of interaction, and in which all quantum gates are defined. The natural choice for our multi-dot array is $H_0 = H_{\text{dot}}$ and $H_1 = H_{\text{ex}}$ as suggested by Eq. (5). Some literatures uses external microwave to define similar rotating frame. Although this approach is intuitive for a single-qubit system, it would be problematic if multiple qubits with different Zeeman energies are involved.

The qubit-frame time evolution $\tilde{U}(\tau)$ is generated by the interaction picture Hamiltonian $U_0(\tau)^\dagger H_1 U_0(\tau)$, but the time-dependence makes direct integration difficult. Here, we take an equivalent approach by reversely rotating the qubit frame,

$$\tilde{U}(\tau) = e^{+i\tau H_0} e^{-i\tau(H_0 + H_1)}. \quad (7)$$

We note that one cannot cancel the H_0 terms, which would require H_0 and H_I to commute. To proceed with the qubit-frame time evolution, we make the assumption that the system works in the non-degenerate regime, where the qubit ground and excited states are well-separated. Specially, the typical Zeeman energy should be much larger than the interdot exchange energy $\varepsilon^Z \gg J$. Notably, this condition is also equivalent to $\|H_0\| \gg \|H_I\|$, allowing the Hamiltonian $H = H_0 + H_I$ to be approached in a perturbative way.

Let us denote the eigenstates and eigenenergies of H as $\{|n'\rangle\}$ and $\{E'_n\}$, which are perturbed from the corresponding eigenstates $\{|n\rangle\}$ and eigenenergies $\{E_n\}$ of H_0 . Here, $|n\rangle$ is simply a direct-product of $|\uparrow\rangle$ and $|\downarrow\rangle$ dot states and E_n is the combination of the relevant Zeeman energies, both can be naturally-defined. To calculate the qubit-frame map $\tilde{U}(\tau)$ in the computational basis, we can calculate the matrix exponential of H in Eq.(7) in terms of the $\{|n'\rangle\}$ states, and then applying a basis transformation to the $\{|n\rangle\}$ -basis. In particular, the diagonal elements of $\tilde{U}(\tau)$ are given by

$$\tilde{U}_{nn}(\tau) = r_{nn}e^{-i\tau\delta E_n} + \sum_{m \neq n} r_{nm}e^{-i\tau(E'_{mn} + \delta E_n)} \quad (8)$$

where $r_{nm} \equiv |\langle n|m' \rangle|^2$, $\delta E_n \equiv E'_n - E_n$ and $E'_{mn} \equiv E'_m - E'_n$. The derivation is exact up to this stage. Next we will make the perturbative assumption, which will allow us to split the sum in Eq.(8) into a major term with $r_{nn} \sim 1$, and many minor terms with $r_{nm} \sim O(J^2)$. By keeping the leading-order effect, we make the approximation,

$$\tilde{U}(\tau) \approx \text{diag}(e^{-i\tau\delta E_1^{(1)}}, e^{-i\tau\delta E_2^{(1)}}, \dots) \equiv \tilde{U}_{\text{ideal}}, \quad (9)$$

where $\delta E_n^{(1)} = \langle n | H_{\text{ex}} | n \rangle$ are the first-order energy corrections. For the most part of this paper, we concern ourselves with the problems of what and how a useful quantum gate can be achieved with \tilde{U}_{ideal} . We attribute the difference between $\tilde{U}(\tau)$ and \tilde{U}_{ideal} as *coherent* errors, whose combined magnitude is should be of higher orders. We will examine these errors in details in Sec. III C. In a sense, we can view quantum gates as first-order effects on the quantum dot array brought by exchange coupling. In comparison, the zeroth order effect defines the qubits while higher order effects are considered as errors.

C. Grid and bond vectors

By definition, \tilde{U}_{ideal} is diagonal in the computational basis. Therefore a convenient way to express the \tilde{U}_{ideal} is to introduce

$$\tilde{U}_{\text{ideal}} = e^{i\tau\Lambda}, \quad (10)$$

where Λ is the diagonal matrix defined by the first-order energy corrections, or simply the vector itself when its

clear from the context. Using first-order perturbation theory, we can explicitly derive

$$\Lambda = \bigoplus_w J_w \text{diag}(|\xi_w\rangle\langle\xi_w|) \equiv \bigoplus_w \Lambda_w, \quad (11)$$

where the Kronecker sum (\oplus) is defined for vectors (matrices) $\mathbf{x} \in A$ and $\mathbf{y} \in B$ in different linear spaces by, $\mathbf{x} \oplus \mathbf{y} = \mathbf{x} \otimes \mathbf{1}_{B \setminus A} + \mathbf{1}_{A \setminus B} \otimes \mathbf{y}$, where $\mathbf{1}_{B \setminus A}$ is the one-vector (or identity matrix) on the difference space $B \setminus A$, and vice versa for $\mathbf{1}_{A \setminus B}$. As Λ depends on all connecting edges of the quantum-dot array while Λ_w depends only on a particular bond, we refer the former as the “grid vector” and later as the “bond vector”. Each bond vector can be explicitly represented in its associated 4-dimensional subspace by

$$\begin{aligned} \Lambda_w &\stackrel{\text{def}}{=} (\frac{1}{2}J_w|s_w|^2, \frac{1}{2}J_w|t_w|^2, \frac{1}{2}J_w|t_w|^2, \frac{1}{2}J_w|s_w|^2) \\ &\equiv (S_w, T_w, T_w, S_w) \end{aligned} \quad (12)$$

where we have introduced the shorthands S_w and T_w for the spin-conserved and spin-flipped tunneling strength.

Despite the simple form of each bond vector, it can be quite involved to calculate the Kronecker sum of all bonds in a large grid. In general, the vector components of Λ are summations of different S_w and T_w terms. The exact expression in terms of these bond strengths depends on the order of qubits and the geometry of the full grid, and there can have many possible ways of connection for a large collection of quantum dots. However, thanks to the structure of the each bond vector, the grid vector always satisfies the reflective symmetric condition,

$$\Lambda = \overleftarrow{\Lambda} \equiv (\overrightarrow{\lambda}, \overleftarrow{\lambda}), \quad (13)$$

where we introduce the right and left over-arrow to represent writing a vector in normal and reserve order respectively. For an N_Q -qubit system, the length of Λ is 2^{N_Q} while the length of λ is 2^{N_Q-1} . This property implies that there are at most one-half independent entries in Λ , defined by the *reduced* grid vector λ .

D. Free phase factors

The DC time evolution under anisotropic exchange is responsible for entangling different spin qubits. To convert the time evolution map into more familiar expressions of quantum gates, we allow additional global phase and local phase gates. We refer these combined phase degrees of freedom as the free phase factors.

Firstly, a global phase factor can be applied to any wave vector without inducing conceivable change of any physical observables. Hence two unitary maps related by an arbitrary global phase factor ϕ_g are completely equivalent, $e^{i\phi_g}U \doteq U$, where the dot-equal symbol is used to represent such equivalence. More importantly, we also allow two unitary gates to differ by local phase gates on individual qubits. The rationale behind such

local phase freedom is that Z -axis rotations can be implemented by the so-called virtual- Z gates in the software level and do not require actual operations on the qubits [61, 62]. This local phase gate freedom is also exploited in original the proposal of two-qubit CZ gate [23]. In this paper, we will assume that such single-qubit Z rotations come at trivial cost of state fidelity or operation time. The phase gate for a single qubit is the operator $Z_\phi = e^{-i(\phi/2)\sigma_z} \doteq \text{diag}(1, e^{i\phi})$. Direct product of single qubit phase gates gives local phase gates for multi-qubits. Combing the global and local phase degree of freedom, we can define a free phase map

$$Z_{\text{free}} \equiv e^{i\phi_g} \bigotimes_j Z_{\phi_j} = e^{i\Phi_F}, \quad (14)$$

where we can associate Z_{free} with a vector Φ_F , as all phases gates are diagonal. The “free vector” Φ_F is a sum of a global phase and a local part $\Phi_F = \phi_g + \Phi_{\text{loc}}$, with the local free vector

$$\Phi_{\text{loc}} \equiv \bigoplus_j (0, \phi_j). \quad (15)$$

We say that a multi-qubit gate G can be intrinsically attained under direct exchange if it is related to the qubit-frame operator \tilde{U}_{ideal} up to free phase factors,

$$\tilde{U}_{\text{ideal}}(\tau_G) = Z_{\text{free}}(\phi_G) G, \quad (16)$$

where ϕ_G is the solution of (global and local) phase factors and τ_G is the time duration for implementing gate G . As both \tilde{U}_{ideal} and Z_{free} are diagonally represented in the computation basis, we are interested in the multi-qubit gates that are also diagonal in the computational space. The unitarity requirement of such gate G implies that the diagonal elements of G are all just phase factors and can be written as

$$G = e^{i\Theta_G}, \quad (17)$$

where the gate vector Θ_G consists of real numbers associated with the gate. Focusing only on the phase factors, we obtain from Eqns. (9, 14, 17) the relation for the vectors,

$$\tau\Lambda = \Theta_G + \Phi_F \mod 2\pi, \quad (18)$$

where the equality is understood in terms of 2π modulus in all the vector components as any extra 2π phase factor contributes trivially.

III. INTRINSIC MULTI-QUBIT GATES

Equipped with the Hamiltonian and phase corrections, in this section we study what multi-qubit gates can be intrinsically achieved on a general spin-qubit grid. We will first consider some specific examples and their potential applications then gives a general theory for identifying the accessible quantum gates.

A. Multi-qubit controlled-phase gates

A particular useful class of quantum gates is the general controlled-phase gates. We require these gates to involve at least one control qubit and at least one target qubit subjecting to phase-shift according to the state of the control qubit(s). Notable examples include the regular controlled-Z (CZ) gate, the Toffoli-type controlled-controlled-Z (CCZ) gate and the parity checker controlled-Z-Z (CZZ) gate. Here we will examine of what gates are achievable and in what kind of geometry can it be achieved.

1. Composition rules

Without loss of generality, we fix the first qubit as the control qubit and label it by ‘C’, with the rest qubits, which may or may not be involved in the gate, labelled by $1, 2, \dots, n \equiv N_Q - 1$. The full Hilbert space is thus spanned by $\{|0\rangle, |1\rangle\}_c \otimes \{|0\rangle, |1\rangle\}_1 \otimes \dots \otimes \{|0\rangle, |1\rangle\}_n$. Setting the first qubit as control implies that the first half of the computational states remain intact under the gate transformation, while the second half is subject to certain phase flips. The gate vector of such controlled-phase gate can be written as

$$\Theta_G = (\mathbf{0}, \boldsymbol{\theta}_G), \quad (19)$$

where the zero vector $\mathbf{0}$ has half the length of Θ_G and we refer the vector $\boldsymbol{\theta}_G$ as the reduced gate vector.

For the above specified qubit labels, the local phase factors comprise a vector $\phi_{\text{loc}} = (\phi_C, \phi_1, \dots, \phi_n) = (\phi_C, \boldsymbol{\phi}_T)$. Note that we use capital and lower-case letter to distinguish the local free vector with the vector of local phase factors. Expanding the free vector over the control qubit according to Eq. (15), we find $\Phi_{\text{loc}} = (\boldsymbol{\Phi}_T, \phi_C + \boldsymbol{\Phi}_T)$, where $\boldsymbol{\Phi}_T$ is the free phase vector for $\boldsymbol{\phi}_T$ only. To further take advantage of the property that the vector Λ is reflectively symmetric, we split all vectors in Eq. (18) into equal halves and equate them separately. This allows us to formulate two equivalent gate composition rules in terms of the reduced phases vectors. An intrinsic gate must satisfy both rules simultaneously. The first is the parity rule,

$$\boldsymbol{\theta}_G = \overleftarrow{\boldsymbol{\Phi}}_T - \overrightarrow{\boldsymbol{\Phi}}_T - \phi_C = L_{N_Q} \boldsymbol{\phi}_{\text{loc}} \mod 2\pi, \quad (20)$$

where we have introduce the parity matrix L_{N_Q} that is uniquely determined by the total number of qubits N_Q . Since $\boldsymbol{\theta}_G$ is 2^{N_Q-1} dimensional but there are only N_Q local phases to vary, a large number of gates are rejected by the parity rule. The parity rule thus offers a straightforward way to examine whether a gate is allowed or not in theory. After solving the required local phase corrections, the next step is to examine the dynamics rule,

$$\tau\boldsymbol{\lambda} = \phi_g + \boldsymbol{\Phi}_T \mod 2\pi, \quad (21)$$

with Φ_T determined by Eq.(20). This equation connects the required local phase corrections to the grid vector. Therefore it determines what type of connectivity of the quantum dots is required for implementing a target gate within finite time.

2. Examples

At this stage, it is helpful to first examine some simple examples of quantum gates.

The simplest case is a two-qubit system. It is well-known that DC evolution under exchange can produce the CZ gate. Here we examine the general controlled-phase gate $CZ_\theta \cong \text{diag}(1, 1, 1, e^{i\theta})$. The parity rule for such gate reads

$$\begin{pmatrix} 0 \\ \theta \end{pmatrix} = \begin{pmatrix} -1 & 1 \\ -1 & -1 \end{pmatrix} \begin{pmatrix} \phi_c \\ \phi_1 \end{pmatrix} \quad \text{mod } 2\pi. \quad (22)$$

Since the parity matrix is invertible, any θ value is allowed. The general solution of local phase factors is given by $\phi_1 = -\frac{1}{2}\theta + k_1\pi$ and $\phi_c = -\frac{1}{2}\theta + (k_1 + 2k_2)\pi$ for $k_1, k_2 \in \mathbb{Z}$. As there is only one possible way of connecting two dots, the reduced grid vector is identified by $\lambda = (S, T)$. Substituting into the dynamics rule, we can obtain the explicit gate time,

$$\tau = \frac{-\theta/2 + n\pi}{T - S}, \quad n \in \mathbb{Z}. \quad (23)$$

Here the integer n is further restricted such at $\tau > 0$.

Increasing the qubit number to three, we have a much more interesting system that can demonstrate many interesting aspects of multi-qubit gates. We first explicitly write down the parity rule for three-qubit gates,

$$\theta_G = \begin{pmatrix} -1 & 1 & 1 \\ -1 & 1 & -1 \\ -1 & -1 & 1 \\ -1 & -1 & -1 \end{pmatrix} \begin{pmatrix} \phi_c \\ \phi_1 \\ \phi_2 \end{pmatrix} \quad \text{mod } 2\pi. \quad (24)$$

The parity matrix is 4×3 . This indicates there are more constraints than the free local phase variables. Hence only a subset of the three-qubit controlled phase can be intrinsically implemented. A striking example prohibit by parity is the CCZ gate. It corresponds to the gate vector $\theta_G = (0, 0, 0, \pi)$. Substituting θ_G into the above equation, we obtain

$$\begin{cases} -\phi_c + \phi_1 + \phi_2 = 2n\pi \\ \phi_c - \phi_1 + \phi_2 = 2m\pi \\ \phi_c + \phi_1 - \phi_2 = 2k\pi \\ \phi_c + \phi_1 + \phi_2 = 2l\pi - \pi \end{cases}, \quad (25)$$

where n, m, k, l are integers. Summing up the first three terms yield the final term on the left-hand-side, but the right-hand-sides suggests the sum is simultaneously even and odd multiple of π , an apparent contradiction.

A class of achievable gate is the $CZ_{\theta_1}Z_{\theta_2}$, which applies conditional phase shifts of θ_1 and θ_2 for qubit 1 and 2. Plugging in the corresponding gate vector $\theta_G = (0, \theta_2, \theta_1, \theta_1 + \theta_2)$ into Eq.(24), one can verify that a consistent solution can be found by

$$\begin{cases} \phi_1 = -\frac{1}{2}\theta_1 + k_1\pi \\ \phi_2 = -\frac{1}{2}\theta_2 + k_2\pi \\ \phi_c = -\frac{1}{2}\theta_1 - \frac{1}{2}\theta_2 + (k_1 + k_2 + 2k_3)\pi \end{cases}, \quad (26)$$

where k_1, k_2, k_3 are arbitrary integers. From local phase solutions, we can determine $\Phi_T = (0, \phi_2, \phi_1, \phi_1 + \phi_2)$. Next, we also need to check if such gate is dynamically allowed. For a three-qubit system, there can have three distinct bonds in the fully-connected setup. And this generalize to $\binom{n}{2}$ bonds in a fully-connected n -qubit system. But here we only consider a one-dimensional array with two connecting bonds. And we can distinguish two possibilities for a three-qubit system—that of linear fashion, where the control and target qubits are connected sequentially in the order of ‘C’-‘1’-‘2’; and the that of stellar fashion, in which the control qubit is placed in the center following ‘1’-‘C’-‘2’. For the stellar geometry, the grid vector can be calculated as

$$\lambda^{(\text{ste})} = (S_1 + S_2, S_1 + T_2, S_2 + T_1, T_1 + T_2). \quad (27)$$

Substituting the grid vectors into Eq.(20), we find that the dynamics condition decouples to separate identities for each bond:

$$\tau(T_1 - S_1) = \phi_1, \quad \tau(T_2 - S_2) = \phi_2, \quad \text{mod } 2\pi. \quad (28)$$

This can be in principle achieved by controlling the tunneling ratio $(T_1 - S_1)/(T_2 - S_2)$. On the other hand, the linear geometry is associated with

$$\lambda^{(\text{lin})} = (S_1 + S_2, S_1 + T_2, T_1 + T_2, S_2 + T_1). \quad (29)$$

Contrary to the previous case, there is no non-trivial solution to the dynamics rule, unless if $\phi_2 = \pi \pmod{2\pi}$. But this would indicate that qubit 2 undergoes a conditional 2π rotation, which is equivalent to a Z gate on the control qubit, and the resulting gate reduces to a two-qubit gate. In particular, if the two bonds are identical, then after time $\tau = \pi/(T - S)$, we have $\phi_c = \phi_2 = \pi$ and $\phi_1 = 0$, the locally-uncorrected time evolution will become joint single-qubit Z gates on both ends:

$$\tilde{U}(\tau) = Z_c \otimes Z_2, \quad (30)$$

which is a non-entangling gate even though the qubits are entangled amidst the time evolution.

3. General multi-qubit control gates

A particular class of quantum gates is naturally allowed by parity. This class has only one control qubit but

allow multiple target qubits, $\text{CZ}_{\theta_1}\text{Z}_{\theta_2} \cdots \text{Z}_{\theta_n}$. In particular, when all controlled-phase factors are π , these become the multi-qubit controlled- Z gates, which have important application in quantum computing algorithms and quantum error correction codes. For such multi-qubit controlled-phase (MQCP) gate, we have the reduced gate vector $\boldsymbol{\theta}_G = (0, \theta_1) \oplus (0, \theta_2) \oplus \cdots \oplus (0, \theta_n)$. After calculating the target free vector and its reverse vector by Eq. (15), we obtain the parity rule

$$\bigoplus_{j=1}^n (0, \theta_j) = \bigoplus_{j=1}^n (\phi_j, -\phi_j) - \phi_c \quad \text{mod } 2\pi. \quad (31)$$

for which we have the solution

$$\begin{cases} \phi_j = -\frac{1}{2}\theta_j \quad \text{mod } \pi \\ \phi_c = \sum_{j=1}^n \phi_j \quad \text{mod } 2\pi \end{cases}. \quad (32)$$

This explicitly proves that such one-control, multi-target gate is allowed by parity.

In comparison, the parity rule requires that the number of control qubits cannot exceed 1. This is already hinted by the three qubit example. We formally prove this theorem in the follows. Without loss of generality, we set the qubit 1 also as the control qubit. This implies that such $\boldsymbol{\theta}_G = (\mathbf{0}, \boldsymbol{\theta}'_G)$, where $\mathbf{0}$ is a zero vector of length 2^{n-1} . Next, we partition both sides of the parity rule into equal halves, yielding

$$\begin{cases} \phi_1 - \phi_c + \bigoplus_{j=2}^n (\phi_j, -\phi_j) = \mathbf{0} \\ -\phi_1 - \phi_c + \bigoplus_{j=2}^n (\phi_j, -\phi_j) = \boldsymbol{\theta}'_G \end{cases} \quad \text{mod } 2\pi \quad (33)$$

Solving this condition, we find the vector $\boldsymbol{\theta}'_G = -2\phi_1$ a constant vector (up to 2π modulus). But such solution in turn suggest that the gate is a controlled-phase between C and 1 instead of a multi-qubit gate with two control qubits, which completes our proof. For this reason, we will only consider the gates with one control qubit when taking about multi-qubit control.

Let us now examine the the dynamics rule for the multi-qubit control gate. As hinted by the three qubit example, it turns out that such gate can be generally implemented in the stellar geometry. In the stellar geometry, the control qubit lives in the center of a cluster, and all other qubits are directly connected to the control qubit via bonds 1, 2, \cdots , n . The reduced grid vector in such case can be worked out as

$$\boldsymbol{\lambda}^{(\text{ste})} = (S_1, T_1) \oplus (S_2, T_2) \oplus \cdots \oplus (S_n, T_n). \quad (34)$$

Substituting the $\boldsymbol{\lambda}$ vector into Eq. (21), we require

$$\bigoplus_j (\tau S_j, \tau T_j) = \phi_g + \bigoplus_j (0, \phi_j), \quad (35)$$

which can be solved by taking $\phi_g = \sum \tau S_j$ and that each bond satisfying

$$\tau(T_j - S_j) = \phi_j = -\frac{1}{2}\theta_j \quad \text{mod } \pi. \quad (36)$$

This solution suggests that such multi-qubit control is also allowed dynamically. This completes the full proof that the multi-qubit controlled phase gates are intrinsic. Of course, we have hitherto only considered the theoretical perspectives and leave out the technical details. From Eq. (36), we see that arbitrary controlled phases can be in principle achieved by controlling the tunnelling strength T_j and S_j for each bond. But as the qubit number scales up, the resources for simultaneously calibrating and controlling all bond can quickly become unmanageable. We will discuss a more robust and scalable scheme to fulfill this dynamics condition in Section IV.

We can also examine the multi-qubit controlled-phase under another type of geometry—the linear geometry. In the linear geometry, the qubits are labeled sequentially from one end to another end of an 1D chain (in a topologically equivalent way), and are connected with near-neighbors. The linear geometry cannot implement a general multi-qubit controlled-phase gate. But there is one exception: For a homogeneous chain with one control and n target qubits, a π -phase can accumulate on both ends $\phi_c = \phi_n = \pi$ but coherently cancels out for other qubits $\phi_1 = \phi_2 = \cdots = \phi_{n-1} = 0$. Such solution is already discussed in the three-qubit example. We can prove the general case with mathematical induction by noting the following recurrence relation

$$\boldsymbol{\lambda}^{(n+1)} = \boldsymbol{\lambda}^{(n)} \otimes (1, 1) + \boldsymbol{\lambda}^{(n-1)} \otimes (S, T, T, S), \quad (37)$$

where $\boldsymbol{\lambda}^{(n)}$ is the the grid vector for chains with n target qubits. In general, the solution to the dynamics rule can be found for

$$\tau = \frac{(2k+1)\pi}{T-S}, \quad k \in \mathbb{Z}. \quad (38)$$

whence the resulting uncorrected time evolution is simply

$$\tilde{U}(\tau) = Z_c \otimes I_1 \otimes I_2 \otimes \cdots \otimes I_{n-1} \otimes Z_n. \quad (39)$$

We remark that the superexchange oscillations observed for boundary states of a spin chain are manifestation of this gate [42, 43]. Such gate might be trivial from the quantum computational perspective, as it is just joint single-qubit Z . But the underlying physics is quite interesting. The final gate does not depend on the length and participating qubits involved in the path connecting the control and the final target qubit. In other words, it has the property of being topologically invariant.

B. General gate decompositions

The MQCP gates stands for only a small fraction of what can be intrinsically achieved on a multi-qubit array. And there can be many different intrinsic gates under different types of dot connectivity. But in fact, all intrinsic gates can be decomposed into simultaneous MQCP gates. As a result, all the conclusions regarding local phase corrections, gate fidelity, and scalable implementations can be directly carried over.

The rationale for the above decomposition theorem is surprisingly simple. Let us re-examine the gate time evolution, which is governed by a grid vector that further decomposes into bond vectors $\Lambda = \otimes_w \Lambda_w$. Despite different bonds can share common dots, when viewed as diagonal matrices, all Λ_w commutes with each other. Hence the time-evolution decomposes automatically onto each bonds

$$\tilde{U}_{\text{ideal}} = \exp\left(i\tau \bigotimes_w \Lambda_w\right) = \prod_w (e^{i\tau \Lambda_w} \otimes I_{w\perp}), \quad (40)$$

where $I_{w\perp}$ is the identity on the orthogonal space of the bond w . The combined gate on the full grid is simply the product of gates on each bonds. The order of this product is irrelevant since all matrices commute.

As a result, we can view the MQCP gates as the product of multiple two-qubit controlled-phase gates with the same control qubit. As illustrated in Fig. 2(a) for a five-qubit example. The single quantum gate with a central qubit controlling multiple target qubits is equivalent to the product of multiple controlled-phase gates. Furthermore, for a general quantum dot array with a given connectivity, we can identify the achievable gate by decomposing the full array into multiple stellar-connected subgroups, each implementing a MQCP gate. The resulting gate may no longer be an MQCP gate. For example, consider the three-qubit ring in Fig. 2(b), the intrinsic gate is a product of three CPhase gates, and no particular qubit can stand out as the control qubit. The total time evolution under such connectivity is equivalent to a product of those MQCP gates. This is demonstrated in Fig. 2(c) for a six-qubit array with two equivalent ways of decomposition.

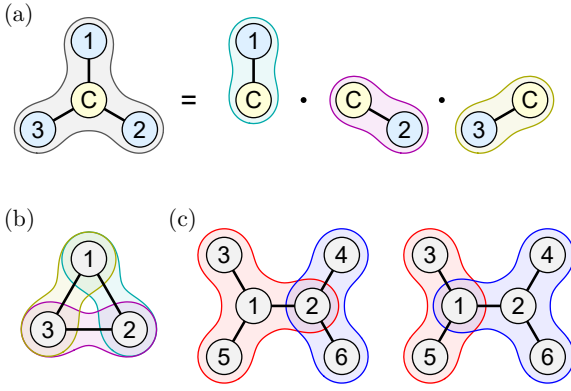


FIG. 2. Decomposition of intrinsic multi-qubit gates based on the dot connectivity. (a) The intrinsic gate for a four-qubit system in stellar configuration is an MQCP gate, which can be decomposed as the Kronecker product of three two-qubit CPhase gates. (b) The intrinsic gate of a three-qubit ring does not contain a control qubit, as the three qubits are totally symmetric to each other. (c) Two different ways of decomposing the same intrinsic gate for a six-qubits array as product of MQCP gates. The resulting local phase corrections are independent of particular choice of decomposition.

Proper local phase corrections are still required for a multi-qubit array to implement a product of MQCP gates. It is straightforward to show that the necessary phase corrections are summations of the phase corrections for each MQCP subgroups. This also explains the local phase identity $\phi_c = \sum_j \phi_j$ for a general MQCP gate, which can be decomposed into multiple two-qubit groups with $\phi_c = \phi_j$. While for more general arrays, there can have multiple viable ways of gate decomposition. Consider the example in Fig. 2(c), we have two different ways of decomposition into MQCP gates. At first sight, this ambiguity seems to give rise to uncertainties in local phase corrections. But it turns out the local phase corrections for a particular qubit only depends on the total tunneling strengths of the bonds connecting to that qubit. Therefore, different ways of decompositions are just equivalent ways of understanding the same gate. For the Fig. 2(c) example, assuming that all bonds are homogeneous and satisfy the condition $(T - S)\tau = \pi/2$, we find $\phi_1 = \phi_2 = 3\pi/2$ and $\phi_3 = \phi_4 = \phi_5 = \phi_6 = \pi/2$ for both decompositions. In general, the necessary local phase factors are found by

$$\phi_j = \sum_{j \in w} \tau(T_w - S_w). \quad (41)$$

C. Fidelity estimations

We have hitherto replaced the actual time evolution in the rotating frame with the ideal time evolution $\tilde{U}(\tau) \approx \tilde{U}_{\text{ideal}}(\tau)$ and considered what can be achievable with \tilde{U}_{ideal} . The difference between the actual and ideal unitary maps is regarded as coherent error. In this section, we examine how much error is brought by making such approximation.

In general, we can characterize quantum gate implementations using the average gate fidelity, defined by averaging the fidelity for output states over all input states. Here, we are concerned with estimating the fidelity loss by replacing \tilde{U} with \tilde{U}_{ideal} . As both are unitary maps with the same dimensionality, the fidelity function can be calculated by

$$F(\tilde{U}, \tilde{U}_{\text{ideal}}) = \frac{d + |\text{tr}(\tilde{U}^\dagger \tilde{U}_{\text{ideal}})|^2}{d(d+1)}, \quad (42)$$

where d is the dimension of the system. A helpful simplification is brought by the fact that \tilde{U}_{ideal} is diagonal in the computational basis: we only need to focus on the diagonal elements of \tilde{U} for calculating the fidelity. Substituting in the diagonal elements in Eq. (8), we can compute the trace product by

$$|\text{tr}(\tilde{U}^\dagger \tilde{U}_{\text{ideal}})| = \left| \sum_{n,m} r_{nm} e^{-i(\tau E'_{mn} + \varphi_n)} \right|, \quad (43)$$

where

$$\varphi_n \equiv \tau(\delta E_n - \delta E_n^{(1)}) = \tau \sum_{k \geq 2} \delta E_n^{(k)}. \quad (44)$$

is the residue phase accumulated in time from the higher-order energy corrections. Using a combination of inequalities, we can estimate a lower bound for the trace-product, hence the gate fidelity by

$$F \geq 1 - \frac{2d}{d+1} \max_n |\varphi_n| - \frac{4}{d+1} \sum_n (1 - r_{nn}). \quad (45)$$

We derive this inequality in the appendix. From this lower bound, we find two major sources of coherent errors. One is the residue phase φ_n accumulated in time. The next is the non-unity component $r_{nn} = |\langle n | n' \rangle|^2 < 1$ of the perturbed eigenstate. Specially, we can apply the non-degenerate perturbation theory to find

$$\varphi_n \simeq \tau \sum_{m \neq n} \frac{\left| \sum_w J_w \langle n | \xi_w \rangle \langle \xi_w | m \rangle \right|^2}{\varepsilon_{Z,n} - \varepsilon_{Z,m}} \quad (46)$$

$$\sum_n (1 - r_{nn}) \simeq \sum_{\substack{n,m \\ n \neq m}} \frac{\left| \sum_w J_w \langle n | \xi_w \rangle \langle \xi_w | m \rangle \right|^2}{(\varepsilon_{Z,n} - \varepsilon_{Z,m})^2}. \quad (47)$$

Although both two terms in Eq. (46) and Eq. (47) seem to be of second order in the exchange energy J , the total evolution time contributes inversely $\tau \propto 1/J$. This makes φ_n first order in J/ε_Z and can be attributed as the dominant source of error. However, it is possible to suppress this type of error by applying *additional* corrections to the local phase values predicted by the first-order theory. This technique is already seen in two-qubit gates, where we have slightly different local phase corrections for the two dots for better fidelity.

In general, a set of extra phase corrections produce the gate, $\tilde{U}' = e^{i\delta\Phi}\tilde{U}$, with

$$\delta\Phi = \delta\phi_g + \bigoplus_j (0, \delta\phi_j), \quad (48)$$

for the compensated free phases $\delta\phi_g$ and $\{\delta\phi_i\}$ similar as those defined in Eq. (14) and Eq. (15). Comparing the fidelity between \tilde{U}' and \tilde{U}_{ideal} , we only need to change the vector of accumulated phases $\varphi = (\varphi_1, \varphi_2, \dots, \varphi_{2^{N_Q}})$ to the compensated values

$$\varphi \rightarrow \varphi' = \varphi - \delta\Phi = \varphi - Ky, \quad (49)$$

where we introduce the coefficient matrix K is for vector $y = (\phi_g, \phi_1, \phi_2, \dots, \phi_{N_Q})$. With the gate fidelity bound by the max norm of the vector φ' , the optimal extra phase corrections and accumulated phases can be determined using theory of Moore-Penrose Pseudoinverse by

$$y = K^+ \varphi, \quad \varphi' = (I - K^+ K) \varphi, \quad (50)$$

for $K^+ \equiv (K^\top K)^{-1} K$ uniquely determined by the system dimension. Combined with optimal values for the

tunneling coefficients, the accumulated phases from second order energies correction $\delta E_n^{(2)}$ may be removed.

To demonstrate the effect of extra phase corrections in practice. We explicitly consider the example of a MQCP gate on linear array of three-qubit (as “1-C-2”). For simplicity, we assume $s_j = i \sin(\theta_j)$ and $t_i = e^{i\eta_j} \sin(\theta_j)$ for the tunneling coefficients for the two bonds $j = 1, 2$ connected to the center qubit, with exchange energies J_1 and J_2 . Applying Eq. (46) and Eq. (50), we find $\varphi' \simeq \varphi_{\text{max}} \times (1, -1, -1, 1, -1, 1, 1, -1)^\top$, with

$$\varphi_{\text{max}} = \tau \frac{J_1 J_2}{8\varepsilon_{Z,2}} \sin(2\theta_1) \sin(2\theta_2) \cos(\eta_1 - \eta_2). \quad (51)$$

The corresponding local phase compensations $\delta\phi_1, \delta\phi_2$ and $\delta\phi_C$ are derived in the appendix. The accumulated phase is much smaller under optimal local phase corrections and can be reduced to higher order in J/ε_Z if the tunneling coefficients further satisfy conditions such as $\theta_j = k\pi/2$ or $\eta_1 - \eta_2 = (k + 1/2)\pi$ for $k \in \mathbb{Z}$.

D. Applications and advantages

The rule of general gate decomposition allows us to conceive other intrinsic multi-qubit gates that can be useful for quantum information processing tasks. Here we construct two simple examples. Hopefully these can inspire more sophisticated discussions in future works.

1. Three-qubit logical Z-gate

The first example is still based on the three-qubit system. But this time we assume all three qubits are all connected to each other, as shown in Fig. 2(b). From the gate decomposition law, the corresponding intrinsic gate can be decomposed as three controlled-phase gates, one for each connecting pair. Assuming that the bonds are homogeneous and that π -phase flips are applied, the combined gate becomes

$$G = (C_1 Z_2) \cdot (C_2 Z_3) \cdot (C_3 Z_1) \hat{=} \text{diag}(1, 1, 1, -1, 1, -1, -1, -1). \quad (52)$$

As a result, the $|000\rangle, |001\rangle, |010\rangle$ and $|100\rangle$ states are unaffected while $|011\rangle, |101\rangle, |110\rangle$ and $|111\rangle$ experience π -phase (sign) flips. In other words, the resulting phase flips distinguishes the majorly $|0\rangle$ states with the majorly $|1\rangle$ states. We can compare this gate with the simple product of single-qubit gates $Z_1 Z_2 Z_3$, which flips the sign of the states $|001\rangle, |010\rangle, |100\rangle$ and $|111\rangle$. Both gates acts the same for $|000\rangle$ and $|111\rangle$, but the later does not respect major voting. Meanwhile, the non-entangling gate $X_1 X_2 X_3$ correctly interchanges the majorly $|0\rangle$ states with the majorly $|1\rangle$ states and also anticommutes with G . Based on this property, this three-qubit system can be considered as a error correction code for bit-flip errors, with the logical $|\bar{0}\rangle$ and logical $|\bar{1}\rangle$ encoded with

states that are majorly $|0\rangle$ and majorly $|1\rangle$. The gate G in Eq. (52) becomes the logical \bar{Z} gate whereas $X_1X_2X_3$ becomes the logical \bar{X} .

2. Simultaneous parity checks

The MQCP gates has important implications for parity measurement. The ability to perform simultaneous parity measurement has import applications in quantum error correction codes.

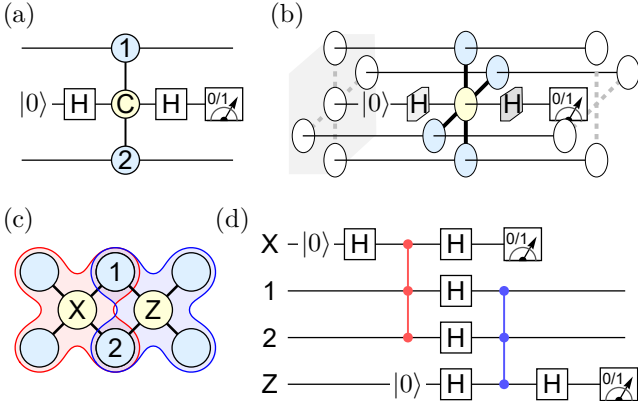


FIG. 3. Example demonstrations of simultaneous parity checks through MQCP gates. (a) The quantum circuit to perform parity check of the Z_1Z_2 operator. The circuit can also be slightly modified to perform parity check of the X_1X_2 operator. (b) A two-dimension parity check circuit that simultaneously check the parity of the four neighboring qubits by application of the $CZ_1Z_2Z_3Z_4$ gate and measurement of the controlled qubit. (c) A basic unit cell of the surface code that involves data qubits with X and Z parity check maps. Both of these maps can be efficiently carried out using MQCP gates. (d) The circuit diagram of the surface code stabilizing cycle for the shared data qubit 1 and 2. The red and blue vertical lines joining three circuit wires are an application of CZ_1Z_2 gates, with the control qubits X and Z as in (c).

In Fig. 3, we demonstrate the applications of MQCP as parity checkers. We first consider implementing the circuit in Fig. 3(a) on a three-qubit array. This circuit involves in preparing the middle qubit in the $|+\rangle$ state by applying a Hadamard gate H to the ground state $|0\rangle$, followed by a CZ_1Z_2 gate with the middle qubit as control, then measuring the control qubit in the $|\pm\rangle$ basis. It can be easily worked out that the measurement outcome will project the other two qubits into ± 1 eigen-spaces of the Z_1Z_2 operator. Essentially, this performs a simultaneous parity check on these two qubits. This circuit can be easily adapted to measure the parity of X_1X_2 operator, by applying two Hadamard gates H_1H_2 after the multi-qubit gate. We only require one multi-qubit gate, compared with the equivalent circuit with two-qubit gate, which requires two CNOT gates. This advantage of MQCP gates as parity checks is especially remarkable for

systems with higher dimension and more complex parity checks. Fig. 3(b) is a direct extension of the circuit in Fig. 3(a) for a two-dimensional array. It can be used to measure the parity of the joint Z - or X -operator of the surrounding target qubits with only one application of MQCP gate. In comparison, the equivalent circuit using two-qubits gates would require 4 applications. and measuring

Simultaneous parity checks can be used as an basic element for constructing surface code. Following an example in Ref. [21], we consider a “unit cell” of surface code with one X and one Z parity check operators. We implement simultaneous parity check gates, shown with the red and blue colored MQCP gates. These two gates are separated by single-qubit Hadamard gates for transforming the $|0/1\rangle$ basis with the $|\pm\rangle$ basis. Fig. 3(d) is a detailed breakdown of such simultaneous parity check for qubit 1 and 2, where the red and blue vertical lines are corresponding MQCP gates. Following this circuit, one can directly verify that the final state for qubit 1 and 2 is stabilized to a simultaneous eigenstate of the Z_1Z_2 and X_1X_2 operator. Compared with equivalent circuit using two-qubit gates, the MQCP gate approach requires significantly less entangling gates, and is capable of measuring the parity of all qubits simultaneously. This could dramatically reduce the error rate associated with the parity measurement process.

3. Fast order reversal

Some quantum computing tasks require reversing the order of a set of states. Notably, this step is involved in quantum Fourier transform, which is necessary for the Shor’s algorithm. Here we assume that these states are hosted in a linear array of spin qubits, the quantum circuit for reversing the array typically breaks down into multiple application of swap gates, which is only allowed for near-neighbors due to restriction in connectivity. In general, flipping an n -qubit array requires $n(n - 1)/2$ near-neighbor swaps, with each swap made up of three CNOT gate (or CZ combined with single-qubit Hadamard gates). Although some swaps can be simultaneously performed, the task still requires $O(n^2)$ steps to accomplish.

The same array reversal task can be achieved with only n multi-qubit gates with π -phase flips on all bonds. By the gate decomposition theory, it can be expressed as

$$G = (C_1Z_2) \cdot (C_2Z_3) \cdots (C_{n-1}Z_n). \quad (53)$$

Consider the following gate sequence that interleaves n such gate with single-qubit Hadamard gates $H = H_1 \otimes H_2 \otimes \cdots \otimes H_n$,

$$R = HGHG \cdots HGH = H(GH)^n. \quad (54)$$

Recall that the array reversal map swaps the state $|\mathbf{a}\rangle$ with $|\overleftarrow{\mathbf{a}}\rangle$ for all the n -digit binary strings \mathbf{a} , e.g.,

$|0011\rangle \leftrightarrow |1100\rangle$. Using the stabilizer group theory, we can show that R differs from the array reversal map only by single-qubit sign flips depending on the parity of the states, i.e,

$$R : |\mathbf{a}\rangle \leftrightarrow p(\mathbf{a}) \times |\overline{\mathbf{a}}\rangle, \quad (55)$$

where $p(\mathbf{a}) = \pm 1$ depends on the number of consecutive 1 in string \mathbf{a} , with even and odd number of consecutive 1 producing $p = +1$ and $p = -1$. For example, the even parity strings “00010” and “01110” contain 0 and 2 occurrence(s) of consecutive 1, compared with the odd-parity strings “00110” and “01111” with 1 and 3 occurrence(s). The matrix representation of R is plotted in Fig. 4 for a linear array of 3, 4 and 5 qubits for demonstration. These extra sign flips can further corrected in the software level with virtual Z gates.

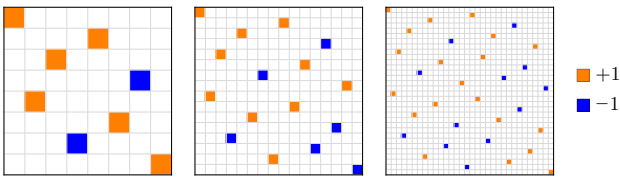


FIG. 4. Matrix representations of the array reversal map R in Eq. (55) for $n = 3, 4, 5$ (from left to right). The matrices differ from the corresponding array reversal maps only by negative signs for some states.

IV. SCALABLE IMPLEMENTATIONS

A. The problem of bond inhomogeneity

Examining the bond strength condition, for example, of the CZZ gate,

$$\begin{cases} \frac{\tau}{2\pi}(T_1 - S_1) = k_1 + \frac{1}{2}, \\ \frac{\tau}{2\pi}(T_2 - S_2) = k_2 + \frac{1}{2}, \end{cases} \quad (56)$$

One way to think of the of intrinsic multi-control gates is to examine the “ k -space” picture. Time evolution trace out a parametric path, which is a straight line with tangent vector $\mathbf{v} = \frac{1}{2\pi}(T_1 - S_1, T_2 - S_2)$ here. The target control gate is specified by a set of lattice points in the k -space, separating by distance 1. The goal for the time evolution is to bump into one of the lattice points, as illustrated in Fig. 5.

In the ideal case, the strength of edge-1 equals that of edge-2, $T_1 - S_1 = T_2 - S_2$. In such case, the path would directly heads towards the first lattice point at $(1/2, 1/2)$, as indicated by the thick green line in Fig. 5(a). This gives the theoretically shortest evolution time of

$$\tau_{\min} = \frac{\pi}{T - S} \quad (57)$$

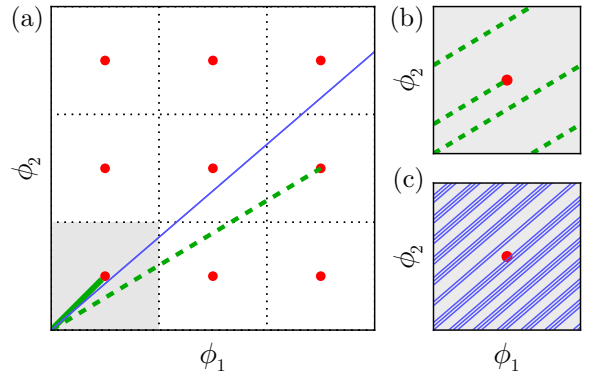


FIG. 5. (a) DC evolution path in the (extended) k -space. The red lattice points represent the target control gate and straight lines represent different evolution paths: the ideal case with identical bonds (thick green line), bonds with mutually rational strengths (dashed green line) and bonds with mutually irrational strengths (thin blue line). (b) and (c), the reduced k -space time evolution for the rational and irrational bonds.

this evolution time is the same as that of two-qubit CZ gate, despite more target qubits are involved.

In reality, due to structural defects and imperfections, it is hard to have completely identical bond strength. Although it is possible to calibrate the bond strength for small degree of freedoms, the issue of inhomogeneity poses a major challenge when the size of qubit chips scale up. From our theory, different coupling strengths are responsible to the different velocity complement of the k -space trajectory. And the time evolution target can be any lattice points offsets by a set of integers. Therefore, even if the bonds are inhomogeneous, it is still possible that the evolution path would bump into some lattice point other than $(1/2, 1/2)$. One such example is plotted with dashed green line in Fig. 5(a), where the time evolution reaches the lattice point $(\frac{5}{2}, \frac{3}{2})$. Apparently, the condition for perfectly attaining a lattice points is that the effective strength $T - S$ between different bonds being rational to each other. In general, the bond strength ratio is irrational, and the evolution path will never perfectly arrive at a lattice point, as illustrated with the thin blue line in Fig. 5(a). This imperfection leads to an error in implementing the target gate. One can still argue that given sufficiently long evolution time, the evolution path can get arbitrarily close to the target point. To understand this property, we consider the reduced k -space indicated by the shaded area in Fig. 5(a). Due to the periodic nature of the target gate, we can fold a full evolution path into the first lattice by simply discarding the integer parts of its vector components. This process is illustrated in Fig. 5(b) and Fig. 5(c) for the rational green path and irrational blue path. For the rational path, the trajectory attain the target point after finite cycles, while for the irrational path, the trajectory will densely cover the whole reduced k -space given enough time.

Although the above discussion is made for a three-qubit system, it holds true for general n -qubit multi control gates. One simply need to replace the two-dimensional k -space picture with a $n - 1$ -dimensional space. We can proceed to estimate an upper bound of the evolution time given target gate infidelity ϵ by

$$\tau \simeq \frac{1}{(n-1)^{1/2} v_{m1}} \Gamma\left(\frac{n}{2}\right) \left(\frac{8/\pi}{\epsilon(n-1)}\right)^{(n-2)/2}. \quad (58)$$

The result is derived by transforming the evolution path into a tube with finite cross-section and ask when does the tube fill the entire reduced k -space [63].

Despite that eventually the target can be achieved. The problem is that the time would take too long following a simple straight path. It is very likely during these time, the qubit will already decohere. Therefore, one must find a way to dramatically accelerate the time evolution. It turns out one can design a controlled path of evolution by pulsing the target qubits.

B. Dynamical calibration: example

The time requirement scales exponentially when the bonds are inhomogeneous. We propose a scheme that will effectively eliminate this issue by “steering the path” in the phase space with fast single-qubit pulses.

Till now, we have only considered time evolutions with time-independent control, i.e., the exchange coupling is turned on and stays constant during the full evolution. This is often termed as DC gates in literatures. We denote the rotating-frame quantum gate at time τ as

$$\tilde{U}_I = e^{i\tau H_0} e^{-i\tau H} \simeq e^{i\tau \Lambda}, \quad (59)$$

where we set time origin at 0 for brevity, $H = H_0 + H_{\text{ex}}$ and the approximation is achieved in the perturbative limit $\|H_0\| \gg \|H_{\text{ex}}\|$ and does not depend on τ .

Going beyond the simple DC-control scheme, let us consider applying a bit-flip pulse X_j to the j -th qubit at time $\tau_1 < \tau$. Assuming the pulse width to be much shorter compared to the time duration for achieving the full multi-qubit gate, we can apply a similar perturbative treatment to calculate the resulting quantum gate

$$\begin{aligned} \tilde{U}_{X_j} &= e^{i\tau H_0} e^{-i(\tau-\tau_1)H} X_j e^{-i\tau_1 H} \\ &\simeq X_j e^{-i\tau_1 \varepsilon_j^Z \sigma_j^Z} \exp[i(\tau - \tau_1) X_j \Lambda X_j + i\tau_1 \Lambda], \end{aligned} \quad (60)$$

where we have used the fact that both $X_j H_0 X_j$ and $X_j \Lambda X_j$ are diagonal to commute and combine matrix exponentials. The first and second terms in Eq. (60) are extra bit-flip and local phase shift for the j th qubit, while the last term is responsible for entangling different qubits. As argued earlier, local phase shifts can be compensated in the software level. The extra bit-flip can be combined with upcoming gates or recovered by applying another

X_j pulse at τ . In the later case, we have

$$\begin{aligned} \tilde{U}_{X_j X_j} &= e^{i\tau H_0} X_j e^{-i\tau_2 H} X_j e^{-i\tau_1 H} \\ &\simeq e^{i\tau_2 \varepsilon_j^Z \sigma_j^Z} \exp[i(\tau_2 X_j \Lambda X_j + \tau_1 \Lambda)], \end{aligned} \quad (61)$$

which produces a different local phase without the extra bit-flip. The entangling part, same in both cases, can be seen as time evolution under the normal grid vector Λ , followed by the conjugated grid vector $X_j \Lambda X_j$ for the period of τ_1 and τ_2 respectively.

Using Eq. (11), we can see that the X_j conjugation is only relevant to the bonds containing dot j ,

$$X_j \Lambda X_j = \sum_{j \in w} J_w \text{diag}(|\xi'_w\rangle \langle \xi'_w| \otimes I_w^\perp) + \sum_{j \notin w} \Lambda_{w'}, \quad (62)$$

where $|\xi'_w\rangle \equiv X_j |\xi_w\rangle$ is the flipped entangled state containing dot j . Effectively, the X_j pulse swap the spin-conserved and spin-flipped tunneling strength $T_w = J|t_w|^2$ and $S_w = J_w|s_w|^2$. For multi-control gates, exchanging T and S tunneling channel of a bond results in a reversal of its effective velocity component. This offers a control possibility where we can design an customize path in the k -space to the target gate by applying single qubit pulses at appropriate intervals.

To better demonstrate this idea, we again consider the three qubit CZZ gate, with bonds connecting the control qubit c to the target qubit j ($j = 1, 2$), on which live the entangled states

$$|\xi_{cj}\rangle = s^* |\uparrow\uparrow\rangle_{cj} + t^* |\uparrow\downarrow\rangle_{cj} - t |\downarrow\uparrow\rangle_{cj} + s |\downarrow\downarrow\rangle_{cj}, \quad (63)$$

where we omit the normalization factor $1/\sqrt{2}$ and the subscripts for t and s . Applying bitflip to the target or control qubit results in,

$$\begin{aligned} X_j |\xi_{cj}\rangle &= t^* |\uparrow\uparrow\rangle_{cj} + s^* |\uparrow\downarrow\rangle_{cj} + s |\downarrow\uparrow\rangle_{cj} - t |\downarrow\downarrow\rangle_{cj}, \\ X_c |\xi_{cj}\rangle &= -t |\uparrow\uparrow\rangle_{cj} + s |\uparrow\downarrow\rangle_{cj} + s^* |\downarrow\uparrow\rangle_{cj} + t^* |\downarrow\downarrow\rangle_{cj}. \end{aligned} \quad (64)$$

In both cases, the spin-conserved and spin-flipped tunneling strength T and S are exchanged. In terms of the k -space velocity $\mathbf{v} = (v_1, v_2)$ in Eq.(56), the X_j pulse flips the velocity component $v_j \rightarrow -v_j$ while the X_c pulse flips both velocity components. Supposing $v_1 > v_2 > 0$, the simplest scheme to overcome bond inhomogeneity is to apply a X_1 pulse at time instant $\tau_1 = \frac{1}{4}(v_1^{-1} + v_2^{-1})$, as illustrated by the path in Fig. 6(a). The total gate time $\tau = 1/2v_2$ is determined by the weaker bond of the two. Alternatively, one can apply two X_1 pulses symmetrically to cancel out the effect of the remaining X gate, show by the path in Fig. 6(b). One step further, one can apply pulses to all three qubits in the order of X_1 , X_2 and X_c , separated by time duration τ_1 , τ_2 and τ_3 respectively. The corresponding rotating-frame evolution can be calculated to be

$$\begin{aligned} \tilde{U}_{X_c X_2 X_1} &= e^{i\tau H_0} e^{-i\tau_4 H} X_c e^{-i\tau_3 H} X_2 e^{-i\tau_2 H} X_1 e^{-i\tau_1 H} \\ &\simeq X_c X_2 X_1 e^{-i\phi'_c \sigma_c^Z} e^{-i\phi'_2 \sigma_2^Z} e^{-i\phi'_1 \sigma_1^Z} e^{i \sum_{k=1}^4 \tau_k \Lambda_k}, \end{aligned} \quad (65)$$

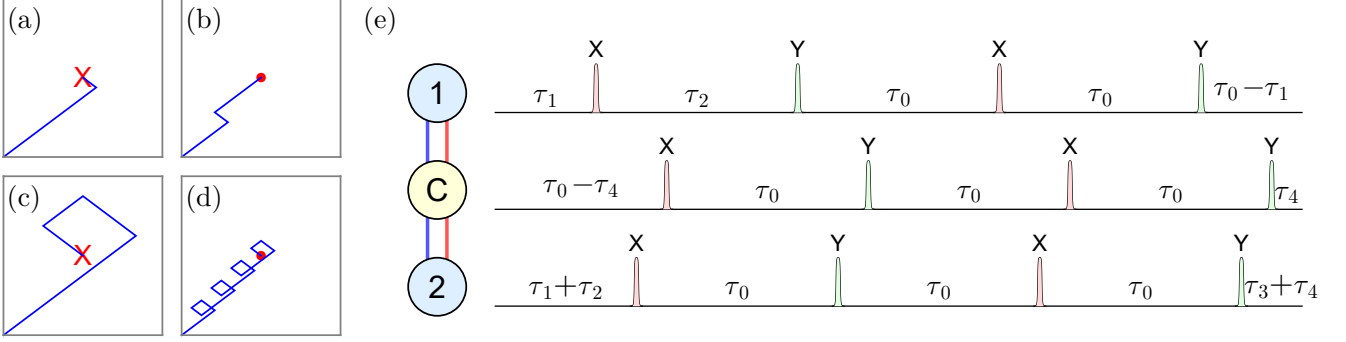


FIG. 6. (a-d): The phase-space path with (a) a single X pulse, (b) a pair of X pulses, (c) three X pulses on all qubits, (d) the $X-Y-X-Y$ dynamical decoupling sequence applied to all qubits. In the figure, the target gate is the red point in the center of the rectangle, while a cross-mark represents that the sequence results in extra X gates to be accounted later. (e): The temporal decomposition of the relevant single qubit pulses in the dynamical decoupling sequence of (d). The dot array is shown in the left inset, followed by X and Y pulses on relevant dots with different separation in time.

where apart from the single-qubit bit-flips $X_c X_2 X_1$, the pulses induce extra local phases $\phi'_c = (\tau_1 + \tau_2 + \tau_3)\varepsilon_c^Z$, $\phi'_2 = (\tau_1 + \tau_2)\varepsilon_2^Z$ and $\phi'_1 = \tau_1\varepsilon_1^Z$. The entangling part is determined by a four-step time evolution, under the effective grid vectors $\Delta_1 = \Delta$, $\Delta_2 = X_1\Delta X_1$, $\Delta_3 = X_2 X_1 \Delta X_1 X_2$, and $\Delta_4 = X_c X_2 X_1 \Delta X_1 X_2 X_c$ for the time duration of τ_1, τ_2, τ_3 , and $\tau_4 \equiv \tau - (\tau_1 + \tau_2 + \tau_3)$ respectively. The k -space path is illustrated in Fig. 6(c).

Compared with a single X_1 pulse, one key advantage of pulsing all three qubits is its potential to be combined with dynamical decoupling (DD), where all three qubits can be protected by decoupling pulses while performing the gate. Specially, let us consider applying the $XYXY$ sequence to each of the qubits. For the system-environment coupling Hamiltonian of H_{SB} , the net effect of the sequence on a single qubit is

$$\begin{aligned} U_{DD} &= Y e^{-i\tau_0 H_{SB}} X e^{-i\tau_0 H_{SB}} Y e^{-i\tau_0 H_{SB}} X e^{-i\tau_0 H_{SB}} \\ &= e^{-i\tau_0(YH_{SB}Y+ZH_{SB}Z+XH_{SB}X+H_{SB})+O(H_{SB})^2}, \end{aligned} \quad (66)$$

The Pauli group twirling results in identity on the system part, hence the pulse sequence can suppress noise effect up to the first order in system-environment coupling. Similar to the X -pulse, a Y -pulse acts on the entangled state by

$$\begin{aligned} Y_j |\xi_{cj}\rangle &= it|\uparrow\uparrow\rangle_{cj} - is|\uparrow\downarrow\rangle_{cj} + is^*|\downarrow\uparrow\rangle_{cj} + it^*|\downarrow\downarrow\rangle_{cj}, \\ Y_c |\xi_{cj}\rangle &= -it^*|\uparrow\uparrow\rangle_{cj} + is^*|\uparrow\downarrow\rangle_{cj} - is|\downarrow\uparrow\rangle_{cj} - it|\downarrow\downarrow\rangle_{cj}. \end{aligned} \quad (67)$$

which also flips the T and S tunneling strength of a particular bond. Based on this similarity between X and Y pulses, we can devise a dynamical calibration scheme that involves interleaved X and Y pulses. The pulsing choice and timing breakdown is illustrated in Fig. 6(e). This dynamical calibration seems like a trivial repetition of the four-staged evolution with X_1, X_2 and X_3 pulses in the k -space, see Fig. 6(d). However, the reduced pulse sequence for each qubit is universal dynamical decoupling sequence. Therefore, each qubit is decoupled from

the environmental interaction by the pulses, while these qubits remain coherently coupled to each other so that a MQCP gate can be performed on them. Hence we see that our dynamical calibration scheme not only is capable of mitigating the inhomogeneity errors, but also allow enhancing the overall qubit quality.

C. Dynamical calibration: general theory

We now present a general theory for the pulsed evolution in the presence of bond inhomogeneity. For a general array of quantum dots with given connection, the intrinsic gate can be decomposed into the product of MQCP gates. The corresponding time evolution reduces to the time evolution in a high dimensional k -spaces according the equation

$$\tau\Delta = \phi = -\frac{1}{2}\theta \mod \pi, \quad (68)$$

where $\Delta = (\Delta_1, \Delta_2, \dots)$ is the vector of effective strength for all the connecting bonds in the array, and $\theta = (\theta_1, \theta_2, \dots)$ is the vector of target phase factors. The π -modulus makes the target gate represents by a high-dimensional lattice of target points. However, the bond strength may differ from ideal values, resulting in unwanted errors in gate implementations. For example, to implement simultaneous multi-qubit controlled-Z gates, all components of θ are equal to π and it is desirable that the effective strength Δ_w for all the participating bonds are equal as well. But the actual bond strengths can vary across the full array.

We can overcome the bond inhomogeneity with recurrent single-qubit pulses. This is done by keeping the dots coupled while inserting single-qubit pulses during the evolution. In general, we can write the qubit-frame

time evolution operator for the pulsed evolution as

$$\tilde{U}_P = e^{i\tau H_0} \cdot e^{-i\tau_N H} P_N e^{-i\tau_{N-1} H} P_{N-1} \cdots P_2 e^{-i\tau_1 H} P_1 e^{-i\tau_0 H}, \quad (69)$$

where the pulse P_n is applied at time instance $\tau_0 + \tau_1 + \cdots + \tau_n$ to some vertex point, within the total duration $\tau = \tau_0 + \tau_1 + \cdots + \tau_N$. The reverse rotation $e^{i\tau H_0}$ in Eq. (69) transforms the lab-frame map to the qubit-frame. The applied pulses are chosen from the Pauli group and they compose into $P_N P_{N-1} \cdots P_1 = Q$. Further introducing an auxiliary set of pulses according to $Q_n = P_n P_{n-1} \cdots P_1$, with $Q_0 = I$ and $Q_N = Q$, we can rewrite the time evolution as

$$\begin{aligned} \tilde{U}_P &= e^{i\tau H_0} Q \prod_{n=0}^N Q_n^\dagger e^{-i\tau_n H} Q_n \\ &\simeq e^{i\tau H_0} Q \prod_{n=0}^N e^{-i\tau_n Q_n^\dagger H_0 Q_n} e^{i\tau_n Q_n^\dagger \Lambda Q_n}, \end{aligned} \quad (70)$$

where we have invoked the perturbative assumption $\|H_0\| \gg \|H_{\text{ex}}\|$ for the approximation in Eq. (70). Since H_0 involves only Pauli-Z operators $\{\sigma_j^Z\}$, conjugation of H_0 by Q_n only selectively flips the signs for the σ_j^Z operators and the resulting matrix is still diagonal in the computational basis. Hence we can commute and combine terms in Eq. (70) and further derive

$$\tilde{U}_P \simeq Q \cdot \bigotimes_j \exp(i\phi'_j \sigma_j^Z) \cdot \prod_{n=0}^N \exp(i\tau_n \Lambda^{(n)}). \quad (71)$$

The time evolution now comprises of three parts. First, an extra Pauli gate Q is introduced by the applied pulses. It can be corrected by applying another gate later in the circuit, or by simply choosing a pulse sequence that composes into the identity. The second part in Eq. (71) is a set of local phase shifts induced by the X_j and Y_j conjugations with σ_j^Z . Assuming $Q_n = \bigotimes_j Q_{nj}$ with $Q_{kj} \in \{I, X, Y, Z\}$ for the j th qubit in the array. For a given pulse scheme, the additional phases is explicitly determined by

$$\phi'_j = \sum_{n=0}^N \frac{1}{2} [\text{sig}(Q_{Nj}) - \text{sig}(Q_{nj})] \varepsilon_j^Z, \quad (72)$$

where $\text{sig}(I) = \text{sig}(Z) = 1$ and $\text{sig}(X) = \text{sig}(Y) = -1$. The extra local phase shifts can be easily corrected with virtual-Z gates and we may ignore them for now. The third part in Eq. (71) describes the entangling dynamics of the array, which is a simple product of $N+1$ time-independent stages. Each stage is generated by a Pauli-conjugated grid vector $\Lambda^{(n)} \equiv Q_n^\dagger \Lambda Q_n$ that can be decomposed as the Kronecker sum

$$\Lambda^{(n)} = \bigoplus_{w=\langle j,k \rangle} Q_{nj}^\dagger Q_{nk}^\dagger \Lambda_w Q_{nj} Q_{nk}, \quad (73)$$

By expressing each bond vector as the diagonal matrix $\Lambda_w \hat{=} \text{diag}(S_w, T_w, T_w, S_w)$, one can directly verify that X or Y conjugations on either dot exchange the T_w and S_w tunneling coefficients, while Λ_w is invariant under Z conjugations. Applying X or Y conjugation to both j and k exchanges the tunneling coefficients twice and leaves the bond vector in its original state. For example, $X_j \Lambda_w X_j = Z_j Y_k \Lambda_w Z_j Y_k \hat{=} \text{diag}(T_w, S_w, S_w, T_w)$ and $X_j Y_k \Lambda_w X_j Y_k = \Lambda_w$. The exchange of tunneling coefficients effectively results in a reversal of velocity component for bond w ,

$$\Delta_w \rightarrow -\Delta_w. \quad (74)$$

For the entire array of dots, an X or Y gate applied to one vertices point will simultaneously reverse the velocities for all bonds connected to that dot. Combined with the geometry of the array, each Q_n specifies the signs for all the bond velocity components. The $\Lambda^{(n)}$ at different stages of evolution are just different combinations of bond velocity components to be integrated with evolution time. This provide a mean to dynamically calibrating the bond strength by properly choosing the time and locations of applied pulses.

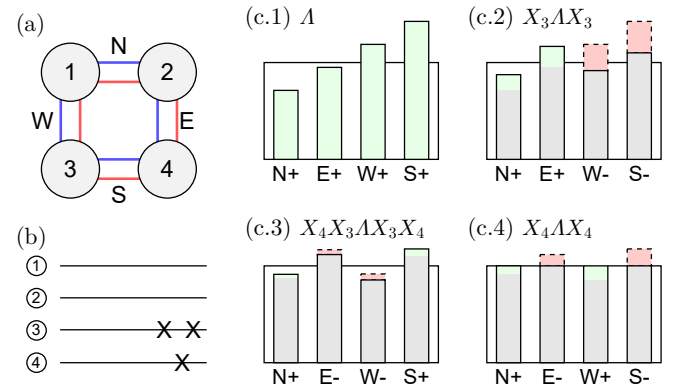


FIG. 7. A minimal dynamic calibration scheme for a rectangle grid. (a) The connectivity structure of the grid, composed of dot 1-4 and bonds N, E, W and S with inhomogeneous (increasing) bond strength. (b) The simplified circuit diagram for the calibration scheme, featuring a total of three X pulses on dot 3 and dot 4. (c.1-4) Break down of the phase factors accumulated in each stage of evolution for the four bonds. The green and red colored bars represent increment and decrement of the accumulated phase in a particular stage, while grey bars are phases accumulated in the previous stage. The effective grid vector for each stage is labeled above the bar charts.

To demonstrate the principles of dynamical calibration, we consider the rectangular grid shown in Fig. 7(a). The dots are connected with four inhomogeneous bonds labeled by ‘N’, ‘E’, ‘W’ and ‘S’. Without loss of generality, we assume $\Delta_N < \Delta_E < \Delta_W < \Delta_S$. The accumulated phases can be dynamically calibrated to reach identical values using the pulses schematically plotted in Fig. 7(b). The time evolution is split into the following four-stage process. At stage 1, the array evolves naturally under the

grid vector Λ . An X pulse is applied to qubit 3 before stage 2. This transforms the grid vector into $X_3\Lambda X_3$ and reverses the velocity components of bond ‘W’ and ‘S’. Hence the accumulated phase for bond ‘W’ and ‘S’ seems a decrease while the phases increase for ‘N’ and ‘W’. This is then followed by an X_4 pulse, transforming the grid vector for the third stage into $X_3X_4\Lambda X_3X_4$ and reversing the velocities for bond ‘E’ and ‘W’. An X_4 pulse is then applied and transforms the grid vector for the final stage as $X_4\Lambda X_4$. The time-integrated phases for the four stages are shown in the bar charts Fig. 7(c-1-4). Assuming that the target phase is ϕ for all the bonds, the time durations τ_0 to τ_3 of the four stages can be solved by

$$\begin{pmatrix} 1 & 1 & 1 & 1 \\ 1 & 1 & -1 & -1 \\ 1 & -1 & -1 & 1 \\ 1 & -1 & 1 & -1 \end{pmatrix} \begin{pmatrix} \tau_0 \\ \tau_1 \\ \tau_2 \\ \tau_3 \end{pmatrix} = \begin{pmatrix} \phi/\Delta_N \\ \phi/\Delta_E \\ \phi/\Delta_W \\ \phi/\Delta_S \end{pmatrix} \quad \text{mod } \pi. \quad (75)$$

We see that the column of the sign matrix corresponds to the signs of the connecting bond ‘N’, ‘E’, ‘W’ and ‘S’ of a particular stage.

Applying our protocol to the most general case, we wish to find an appropriate pulse scheme to calibrate the bond strength for any quantum dot array with arbitrary connection. Apparently, if the array is loopless, such as the ones in Fig. 2, it is possible to reverse each bond independently. A pulse scheme to calibrate all bonds can be easily constructed. If the array topology involves loops, such as the rectangular grid example in Fig. 7, it is generally impossible to reverse all bonds independently. There, one must adopt combinations of different bond reversal schemes to find consistent solutions for the pulse locations and intervals. Here we prove that there is always an appropriate pulse scheme for the fully connected array. Note that this automatically indicates that an array with arbitrary connection can be calibrated as well.

To study the Pauli group conjugations $\{Q\Lambda Q\}$, it suffices to only consider assigning X gates to the fully connected dot array. A particular assignment of X gates, flips the bond velocities $(\Delta_1, \Delta_2, \Delta_3, \dots)$ according to an assignment vector, e.g., $\mathbf{a}_k = (+1, -1, +1, \dots)^\top$ with $|\mathbf{a}_k| = n(n-1)/2 \equiv N_b$ for a fully connected array of n dots. There are 2^n distinctive ways of assigning X gates to the vertices, but different assignments can lead to same bond reversal scheme. We assume that there are at least N_a linearly independent assignment vectors. The pulses intervals are solved in an equation similar to Eq. (75),

$$\begin{pmatrix} | & | & & | \\ \mathbf{a}_1 & \mathbf{a}_2 & \cdots & \mathbf{a}_{N_a} \\ | & | & & | \end{pmatrix} \begin{pmatrix} \tau_1 \\ \tau_2 \\ \vdots \\ \tau_{N_a} \end{pmatrix} = \begin{pmatrix} \tilde{\phi}_1 \\ \tilde{\phi}_2 \\ \vdots \\ \tilde{\phi}_{N_b} \end{pmatrix} \quad \text{mod } \pi, \quad (76)$$

where $\tilde{\phi}_n \equiv \phi_n/\Delta_n$ is the effective bond phase to be accumulated. If $N_a \geq N_b$, i.e., there are same or more linearly independent assignment schemes than the number of bonds, the pulse intervals can be found by solving

this under-determined set of equations. Moreover, the π modulus guarantees that the pulse intervals can always be non-negative $\tau_n \geq 0$. It is straightforward to check that indeed $N_a = 4 > N_b = 3$ for a fully connected triple-dot array. We can prove $N_a > N_b$ for arbitrary array using mathematical induction. Assuming this inequality holds for an n -dot array, we consider a similar condition to Eq. (76) for an array with $n+1$ dots. By adding a dot to the array, n additional bonds are created. We collect the signs for these extra bonds by the $\{\mathbf{b}_k\}$ vectors for the k th assignment of X gates. We now have N_a assignments with the additional dot unchanged and N_a assignments with an X gate applied to the additional dot. These two states should have opposite signs for the extra bonds. In other words, we can write down the following matrix for the assignment vectors,

$$\left(\begin{array}{cccc|cccc} \mathbf{a}_1 & \mathbf{a}_2 & \cdots & \mathbf{a}_{N_a} & \mathbf{a}_1 & \mathbf{a}_2 & \cdots & \mathbf{a}_{N_a} \\ \mathbf{b}_1 & \mathbf{b}_2 & \cdots & \mathbf{b}_{N_a} & -\mathbf{b}_1 & -\mathbf{b}_2 & \cdots & -\mathbf{b}_{N_a} \end{array} \right). \quad (77)$$

Since the column vectors $\{\mathbf{a}_k\}$ are linearly independent by assumption, the extended column vectors $\{(\mathbf{a}_k, \pm \mathbf{b}_k)\}$ must also be linearly independent. Hence when n is increased by one,

$$N_a^{(n+1)} \geq 2N_a^{(n)} = n(n-1) \geq \frac{(n+1)n}{2} = N_b^{(n+1)} \quad (78)$$

for $n \geq 3$. This proves our induction hypothesis.

D. Tunable connectivity with SOI

The typical methods to switch on-and-off the interaction between neighboring spins require either biasing the dot chemical potentials or lowering the tunneling barrier between neighboring dots. In essence, these methods are can be viewed as the modulation of the exchange coupling energy J . This approach works well for two qubit systems, as verified by recent progresses reporting high fidelity figures. However, there are two problems that can hinder the wider application of such approach. First, the interdot coupling cannot be completely cut-off. Experimentally, J is modulated over several order of magnitudes to distinguish the “on” and “off” state. The residue coupling at “off” state will result in errors that accumulate through the circuit. Second, such method does not scale well in terms of the control resources. Modulating the voltage of one particular gate electrode necessarily impact the the exchange coupling of all surrounding dots. As a result, the voltages on many gate electrodes must be simultaneous adjusted. The knowledge of how all the gates should synchronously change is obtained through prior calibration stage. One can imagine the tremendous efforts required to calibrate and accurately control the interdot coupling in a quantum chip with millions of qubits. A viable solution to this issue is to introduce tunable couplers between dots, such as superconducting Josephson junctions or transmon qubits [64]. Here we propose a

whole new approach to control interdot coupling based on the theory developed in this work.

One key ingredient in our theory is the inclusion of spin-orbital coupling. This effect result in an additional spin-flipping channeling when tunneling among dots. However, as suggested by Eq. (36), these two channels act destructively to constitute an effective bond velocity

$$\Delta_w = T_w - S_w = \frac{1}{2} J_w (|t_w|^2 - |s_w|^2). \quad (79)$$

The typical methods to control inter-qubit coupling are centered around controlling the exchange energy J_w . Here we see that it is also possible to control the effective velocity by adjusting the ratio between $|t_w|$ and $|s_w|$. In particular, when $|t_w| = |s_w|$, no phase difference can accumulate across the bond and the bond can be seen as completely cut off. We note that the effective bond velocity can be interpret as an effective exchange energy that can take on negative values, in which the energy relation between spin singlet and triplet states are reversed. Such phenomenon have been reported in studies on few-electron coupled quantum dots [65, 66].

We can distinguish between the coupling and connectivity of two dots. Spin on two dots is coupled if the exchange energy is non-zero, while they are considered connected only if the effective bond velocity is non-zero. By tuning the relative strength between $|t_w|$ and $|s_w|$ while keeping the exchange energy finite, one can control the connectivity with always-on coupling.

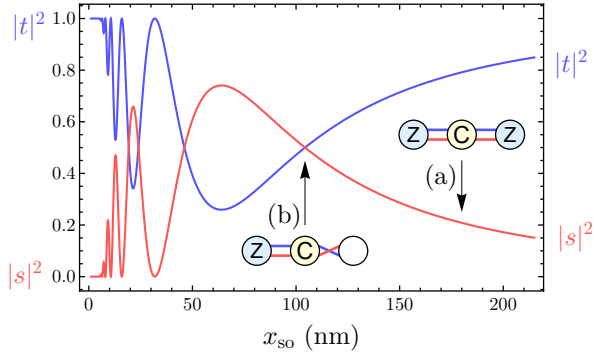


FIG. 8. Dependence of the spin-conserved and spin-flipped tunneling fraction $|t|^2$ and $|s|^2$ on the spin-orbit length x_{SO} for a typical quantum dot array system. The bond connectivity can be controlled by tuning the relative strength between spin-conserved and spin flipped channel. In the subsets, we considered tuning the SOI strength for the right bond in a three-qubit array. We identify the (a) “on” status and (b) “off” status of this bond based on the effective bond velocity. This change of status can be achieved even though the coupling energy J remains unchanged.

Experimentally, both t_w and s_w are dependent on the SOI strength and magnetic field angle on the bond w . It is known that the SOI strength can be continuously tuned by varying the electric field strength. Hence for

static and global the magnetic field, it is possible to control the SOI strength of a particular bond by changing the local electric field. Extra capacitor structure may be involved to suppress crosstalk and enable such precise control. Current spin qubit devices demonstrating such gate tunability is in [67] and also in [68]. For small SOI coupling $x_{SO} \gg 2d$, the interdot tunneling is dominated by the spin-conserved process. As the SOI strength increases (x_{SO} decreases), $|s|^2$ picks up and will come across the decreasing $|t|^2$ at some point. This cross point always exists for magnetic field angle $\pi/4 < \theta_B < 3\pi/4$ and define the “off” state of the relevant bond. In Fig. 8, we plotted the dependence of $|t|^2$ and $|s|^2$ on the spin-orbit length x_{SO} , for a system with interdot spacing $2d = 100$ nm, characteristic Bohr radius $x_0 = 10$ nm and the angle between magnetic field and SOI vector $\theta_B = \pi/3$. Assuming that we are varying the SOI strength for the second bond in a three-qubit array. The insets in Fig. 8 show the intrinsic gates for the (a) “on” state and (b) “off” state of the second bond, where we use parallel lines to indicate an open bond with finite velocity and cross lines to indicate a closed bond with zero velocity. In state (a), the effective velocities for the two bonds are identical $\Delta_1 = \Delta_2$, and the qubits experience a CZZ gate after time evolution $\tau = \pi/\Delta_1$. While in state (b), the same time evolution only induces a CZ gate between the left two qubits—as if the second bond is disconnected. This property holds for general many-qubit arrays. A particular bond can appear disconnected if the spin-conserved and spin-flipped tunneling strength through that bond are equal.

V. CONCLUSION

This article is a detailed theoretical study of the set of intrinsic multi-qubit gates implemented on spin qubit arrays. Our study involves multiple key aspects such as multi-qubit gate dynamics, fidelity estimation and optimizations, advantages in application, scalable calibration with pulse-protected evolution.

We start out from a general model of a spin qubit chip defined by quantum dot array. To describe the dynamics of the half-filling computational subspace, we adopt an effective Hamiltonian that features representing exchange interaction with entangled states on qubit pairs. The entangled states are associated with tunnel-coupled quantum dots and determined by the spin-conserved and spin-flipped tunneling coefficients, which can be further used to define relevant bond vectors for connecting dots. Using first order perturbation theory, we find the time evolution map in the qubit rotating frame is defined by the grid vector of the quantum dot array, which is the Kronecker sum of all the bond vectors. Intrinsic multi-qubit gates is identified with these rotating frame maps in combination with global and local phase gauges.

Applying the gate composition law to general quantum dot arrays, we identify an important class of gates, multi-qubit controlled phase gates, and show that these

gates can be intrinsically achieved by quantum dots arranged in stellar geometry. We then show that all intrinsic multi-qubit gates can be decomposed as simultaneous products of multi-qubit controlled phase gates, and that the local phase correction are determined by the connecting bonds to each dot. We estimate the gate fidelity of these intrinsic gates by deriving an analytical lower bound for the coherent fidelity loss from higher order perturbation terms. It is found that the coherent fidelity is mostly limited by the accumulated phase shifts from second order energy perturbations. The loss in fidelity due to accumulated phase shifts can be effectively suppressed by applying additional local phase corrections obtained from a systematic algorithm. And the fidelity of optimally phase-corrected gates can be further improved by working in parametric sweet spots of the interdot tunneling coefficients. To showcase the advantages of intrinsic multi-qubit gates, we discuss some examples of their application in quantum error correction code, simultaneous

parity measurement and fast array array reversal.

Finally, we examine the problem of bond inhomogeneity necessarily encountered by scaling up the system size. We proposed a theoretical scheme in which the bond strengths are dynamically calibrated with fast pulses. After considering specific examples and show its compatibility with dynamical decoupling, we show that such dynamical calibration protocol can be applied for general array with arbitrary connectivity.

ACKNOWLEDGMENTS

This work is supported by the Beijing Postdoctoral Research Foundation (Grant No. 2023-zz-050), the National Natural Science Foundation of China (Grant Nos. 92165208 and 11874071) and the Key-Area Research and Development Program of Guangdong Province (Grant No. 2020B0303060001).

-
- [1] D. Loss and D. P. DiVincenzo, *Physical Review A* **57**, 120 (1998).
- [2] F. A. Zwanenburg, A. S. Dzurak, A. Morello, M. Y. Simmons, L. C. L. Hollenberg, G. Klimeck, S. Rogge, S. N. Coppersmith, and M. A. Eriksson, *Reviews of Modern Physics* **85**, 961 (2013).
- [3] C. Kloeffel and D. Loss, *Annual Review of Condensed Matter Physics* **4**, 51 (2013).
- [4] G. Burkard, T. D. Ladd, A. Pan, J. M. Nichol, and J. R. Petta, *Reviews of Modern Physics* **95**, 025003 (2023).
- [5] L. M. K. Vandersypen and M. A. Eriksson, *Physics Today* **72**, 38 (2019).
- [6] A. Chatterjee, P. Stevenson, S. De Franceschi, A. Morello, N. P. de Leon, and F. Kuemmeth, *Nature Reviews Physics* **3**, 157 (2021).
- [7] P. Stano and D. Loss, *Nature Reviews Physics* **4**, 672 (2022).
- [8] A. Mills, C. Guinn, M. Feldman, A. Sigillito, M. Gulans, M. Rakher, J. Kerckhoff, C. Jackson, and J. Petta, *Physical Review Applied* **18**, 064028 (2022).
- [9] K. Wang, G. Xu, F. Gao, H. Liu, R.-L. Ma, X. Zhang, Z. Wang, G. Cao, T. Wang, J.-J. Zhang, D. Culcer, X. Hu, H.-W. Jiang, H.-O. Li, G.-C. Guo, and G.-P. Guo, *Nature Communications* **13**, 206 (2022).
- [10] L. C. Camenzind, S. Geyer, A. Fuhrer, R. J. Warburton, D. M. Zumbühl, and A. V. Kuhlmann, *Nature Electronics* **5**, 178 (2022).
- [11] A. Noiri, K. Takeda, T. Nakajima, T. Kobayashi, A. Sammak, G. Scappucci, and S. Tarucha, *Nature* **601**, 338 (2022).
- [12] X. Xue, M. Russ, N. Samkharadze, B. Undseth, A. Sammak, G. Scappucci, and L. M. K. Vandersypen, *Nature* **601**, 343 (2022).
- [13] M. F. Gonzalez-Zalba, S. De Franceschi, E. Charbon, T. Meunier, M. Vinet, and A. S. Dzurak, *Nature Electronics* **4**, 872 (2021).
- [14] A. M. J. Zwerver, T. Krähenmann, T. F. Watson, L. Lampert, H. C. George, R. Pillarisetty, S. A. Bojarski, P. Amin, S. V. Amitonov, J. M. Boter, R. Caudillo, D. Correas-Serrano, J. P. Dehollain, G. Droulers, E. M. Henry, R. Kotlyar, M. Lodari, F. Lüthi, D. J. Michalak, B. K. Mueller, S. Neyens, J. Roberts, N. Samkharadze, G. Zheng, O. K. Zietz, G. Scappucci, M. Veldhorst, L. M. K. Vandersypen, and J. S. Clarke, *Nature Electronics* **5**, 184 (2022).
- [15] N. W. Hendrickx, W. I. L. Lawrie, M. Russ, F. van Riggelen, S. L. de Snoo, R. N. Schouten, A. Sammak, G. Scappucci, and M. Veldhorst, *Nature* **591**, 580 (2021).
- [16] W. I. L. Lawrie, M. Rimbach-Russ, F. van Riggelen, N. W. Hendrickx, S. L. de Snoo, A. Sammak, G. Scappucci, J. Helsen, and M. Veldhorst, *Nature Communications* **14**, 3617 (2023).
- [17] F. Borsoi, N. W. Hendrickx, V. John, M. Meyer, S. Motz, F. van Riggelen, A. Sammak, S. L. de Snoo, G. Scappucci, and M. Veldhorst, *Nature Nanotechnology* **19**, 21 (2024).
- [18] X. Zhang, E. Morozova, M. Rimbach-Russ, D. Jirovec, T.-K. Hsiao, P. C. Fariña, C.-A. Wang, S. D. Oosterhout, A. Sammak, G. Scappucci, M. Veldhorst, and L. M. K. Vandersypen, Universal control of four singlet-triplet qubits (2023), arXiv:2312.16101 [cond-mat.mes-hall].
- [19] A. Yu. Kitaev, *Annals of Physics* **303**, 2 (2003).
- [20] R. Raussendorf and J. Harrington, *Physical Review Letters* **98**, 190504 (2007).
- [21] A. G. Fowler, M. Mariantoni, J. M. Martinis, and A. N. Cleland, *Physical Review A* **86**, 032324 (2012).
- [22] A. Barenco, C. H. Bennett, R. Cleve, D. P. DiVincenzo, N. Margolus, P. Shor, T. Sleator, J. A. Smolin, and H. Weinfurter, *Physical Review A* **52**, 3457 (1995).
- [23] T. Meunier, V. E. Calado, and L. M. K. Vandersypen, *Physical Review B* **83**, 121403 (2011).
- [24] M. Veldhorst, C. H. Yang, J. C. C. Hwang, W. Huang, J. P. Dehollain, J. T. Muonen, S. Simmons, A. Laucht, F. E. Hudson, K. M. Itoh, A. Morello, and A. S. Dzurak, *Nature* **526**, 410 (2015).
- [25] T. F. Watson, S. G. J. Philips, E. Kawakami, D. R. Ward, P. Scarlino, M. Veldhorst, D. E. Savage, M. G.

- Lagally, M. Friesen, S. N. Coppersmith, M. A. Eriksson, and L. M. K. Vandersypen, *Nature* **555**, 633 (2018).
- [26] D. M. Zajac, A. J. Sigillito, M. Russ, F. Borjans, J. M. Taylor, G. Burkard, and J. R. Petta, *Science* **359**, 439 (2018).
- [27] M. Russ, D. M. Zajac, A. J. Sigillito, F. Borjans, J. M. Taylor, J. R. Petta, and G. Burkard, *Physical Review B* **97**, 085421 (2018).
- [28] M. Rimbach-Russ, S. G. J. Philips, X. Xue, and L. M. K. Vandersypen, *Quantum Science and Technology* **8**, 045025 (2023).
- [29] Y.-H. Wu, L. C. Camenzind, A. Noiri, K. Takeda, T. Nakajima, T. Kobayashi, C.-Y. Chang, A. Sammak, G. Scappucci, H.-S. Goan, and S. Tarucha, Hamiltonian phase error in resonantly driven cnot gate above the fault-tolerant threshold (2023), arXiv:2307.09031 [cond-mat.mes-hall].
- [30] X. Gu, J. Fernández-Pendás, P. Vikstål, T. Abad, C. Warren, A. Bengtsson, G. Tancredi, V. Shumeiko, J. Bylander, G. Johansson, and A. F. Kockum, *PRX Quantum* **2**, 040348 (2021).
- [31] L. Isenhower, M. Saffman, and K. Mølmer, *Quantum Information Processing* **10**, 755 (2011).
- [32] M. Khazali and K. Mølmer, *Physical Review X* **10**, 021054 (2020).
- [33] D. Yu, W. Zhang, J. ming Liu, S. Su, and J. Qian, Spheroidal-structure-based multi-qubit toffoli gate via asymmetric rydberg interaction (2020), arXiv:2007.11938 [quant-ph].
- [34] J. T. Young, P. Bienias, R. Belyansky, A. M. Kaufman, and A. V. Gorshkov, *Physical Review Letters* **127**, 120501 (2021).
- [35] N. Chancellor, S. Zohren, and P. A. Warburton, *npj Quantum Information* **3**, 1 (2017).
- [36] T. Liu, B.-Q. Guo, C.-S. Yu, and W.-N. Zhang, *Optics Express* **26**, 4498 (2018).
- [37] E. Bahnsen, S. Rasmussen, N. Loft, and N. Zinner, *Physical Review Applied* **17**, 024053 (2022).
- [38] S. E. Rasmussen, K. Groenland, R. Gerritsma, K. Schoutens, and N. T. Zinner, *Physical Review A* **101**, 022308 (2020).
- [39] J. D. A. Espinoza, K. Groenland, M. Mazzanti, K. Schoutens, and R. Gerritsma, *Physical Review A* **103**, 052437 (2021), arxiv:2010.08490 [quant-ph].
- [40] M. J. Gullans and J. R. Petta, *Physical Review B* **100**, 085419 (2019).
- [41] K. Takeda, A. Noiri, T. Nakajima, T. Kobayashi, and S. Tarucha, *Nature* **608**, 682 (2022).
- [42] H. Qiao, Y. P. Kandel, K. Deng, S. Fallahi, G. C. Gardner, M. J. Manfra, E. Barnes, and J. M. Nichol, *Physical Review X* **10**, 031006 (2020).
- [43] H. Qiao, Y. P. Kandel, S. Fallahi, G. C. Gardner, M. J. Manfra, X. Hu, and J. M. Nichol, *Physical Review Letters* **126**, 017701 (2021).
- [44] F. R. Braakman, P. Barthelemy, C. Reichl, W. Wegscheider, and L. M. K. Vandersypen, *Nature Nanotechnology* **8**, 432 (2013).
- [45] J. Knörzer, C. J. van Diepen, T.-K. Hsiao, G. Giedke, U. Mukhopadhyay, C. Reichl, W. Wegscheider, J. I. Cirac, and L. M. K. Vandersypen, *Physical Review Research* **4**, 033043 (2022).
- [46] D. P. DiVincenzo, D. Bacon, J. Kempe, G. Burkard, and K. B. Whaley, *Nature* **408**, 339 (2000).
- [47] J. Levy, *Physical Review Letters* **89**, 147902 (2002).
- [48] Q. Li, L. Cywiński, D. Culcer, X. Hu, and S. Das Sarma, *Physical Review B* **81**, 085313 (2010).
- [49] R. E. Throckmorton and S. Das Sarma, *Physical Review B* **103**, 165431 (2021).
- [50] G. X. Chan, P. Huang, and X. Wang, *Physical Review B* **108**, 035402 (2023).
- [51] J. Qi, Z.-H. Liu, and H. Xu, *New Journal of Physics* **26**, 013012 (2024).
- [52] L. Viola, E. Knill, and S. Lloyd, *Physical Review Letters* **82**, 2417 (1999).
- [53] L. Viola, S. Lloyd, and E. Knill, *Physical Review Letters* **83**, 4888 (1999).
- [54] K. Khodjasteh and D. A. Lidar, *Physical Review Letters* **95**, 180501 (2005).
- [55] V. N. Golovach, M. Borhani, and D. Loss, *Physical Review B* **74**, 165319 (2006).
- [56] F. N. M. Froning, L. C. Camenzind, O. A. H. van der Molen, A. Li, E. P. A. M. Bakkers, D. M. Zumbühl, and F. R. Braakman, *Nature Nanotechnology* **16**, 308 (2021).
- [57] E. Kawakami, T. Jullien, P. Scarlino, D. R. Ward, D. E. Savage, M. G. Lagally, V. V. Dobrovitski, M. Friesen, S. N. Coppersmith, M. A. Eriksson, and L. M. K. Vandersypen, *Proceedings of the National Academy of Sciences* **113**, 11738 (2016).
- [58] M. Imada, A. Fujimori, and Y. Tokura, *Reviews of Modern Physics* **70**, 1039 (1998).
- [59] S. Yang, X. Wang, and S. Das Sarma, *Physical Review B* **83**, 161301 (2011).
- [60] A. Bogan, S. Studenikin, M. Korkusinski, L. Gaudreau, P. Zawadzki, A. S. Sachrajda, L. Tracy, J. Reno, and T. Hargett, *Physical Review Letters* **120**, 207701 (2018).
- [61] L. M. K. Vandersypen, *Rev. Mod. Phys.* **76**, 33 (2004).
- [62] D. C. McKay, C. J. Wood, S. Sheldon, J. M. Chow, and J. M. Gambetta, *Physical Review A* **96**, 022330 (2017).
- [63] V. Gimeno and J. M. Sotoca, *Journal of Physics A: Mathematical and Theoretical* **50**, 185302 (2017).
- [64] G.-H. Liang, X.-H. Song, C.-L. Deng, X.-Y. Gu, Y. Yan, Z.-Y. Mei, S.-L. Zhao, Y.-Z. Bu, Y.-X. Xiao, Y.-H. Yu, M.-C. Wang, T. Liu, Y.-H. Shi, H. Zhang, X. Li, L. Li, J.-Z. Wang, Y. Tian, S.-P. Zhao, K. Xu, H. Fan, Z.-C. Xiang, and D.-N. Zheng, Tunable Coupling Architectures with Capacitively Connecting Pads for Large-Scale Superconducting Multi-Qubit Processors (2023), arxiv:2306.05312 [quant-ph].
- [65] F. Martins, F. K. Malinowski, P. D. Nissen, S. Fallahi, G. C. Gardner, M. J. Manfra, C. M. Marcus, and F. Kuemmeth, *Physical Review Letters* **119**, 227701 (2017).
- [66] K. Deng, F. A. Calderon-Vargas, N. J. Mayhall, and E. Barnes, *Physical Review B* **97**, 245301 (2018).
- [67] S. Bosco, B. Hetényi, and D. Loss, *PRX Quantum* **2**, 010348 (2021).
- [68] H. Liu, T. Zhang, K. Wang, F. Gao, G. Xu, X. Zhang, S.-X. Li, G. Cao, T. Wang, J. Zhang, X. Hu, H.-O. Li, and G.-P. Guo, *Physical Review Applied* **17**, 044052 (2022).